NON-DESTRUCTIVE EVALUATION USING GUIDED WAVES IN PIPE-LIKE STRUCTURES

By

Jingjun Shen

A THESIS

Submitted to
Michigan State University
in partial fulfillment of the requirements
for the degree of

MASTER OF SCIENCE

Civil Engineering

2012

ABSTRACT

NON-DESTRUCTIVE EVALUATION USING GUIDED WAVES IN PIPE-LIKE STRUCTURES

By

Jingjun Shen

For the last hundred years, rapid development in economy and engineering have accelerated the construction of large amount of different types of civil structures, machines, and airplanes. As time goes by, those structures and machines have deteriorated and become unable to perform their designed functions due to the defects generated during their service lives. To test the integrity of structures and evaluate their health states, in the past several decades, many methods has been developed and utilized. Ultrasonic guided waves have been utilized for accurate diagnosis of the structures that have thin structural components because of their good performance in long distance propagation and sensitivity to defects in the structures. In this thesis, wave propagations excited by surface-mounted instruments such as PZT and transducer rings attached on an infinite isotropic hollow cylinder are investigated. A mathematical model of the wave propagation system is studied both analytically and numerically. A detailed derivation of the characteristic equation for pipes is conducted, and the development of waves is simulated using the finite element method (FEM). Compared with the analytical results, the accuracy of the numerical modeling is verified, and Lamb wave propagation in pipes with defects is studied as well. By parametric study, the influence of the defect depth on the received signals is investigated.

ACKNOWLEDGMENTS

It is a pleasure to thank those who made this thesis possible. I would like to thank my advisor Professor Jung-Wuk Hong, who has helped and supported me throughout my master's study. I am grateful to his patient guidance, and priceless and insightful advices on every stage of my study, from the early stage when I chose my research topic to finishing up this thesis. Without his encouragement and help, I cannot complete this thesis. I am also deeply indebted to Professors Lalita Udpa and Venkatesh Kodur for their inspirations and encouragements through out my research and writing of this thesis.

I want to thank Department of Civil and Environmental Engineering and all my colleague for their help in my research work and my life at MSU. Especially I want to thank Wenyang Liu. We discussed on my research and he inspired me significantly on how to realize my expectations of my research. His suggestions on my research helped me to complete the thesis.

A special thank goes to my family and my friends, especially Mr. Jun He and Ms. Jiaxun Yu, for their undivided support and encouragement during my master's studies. Without their sincere love and support, I would not be able to complete my thesis.

TABLE OF CONTENTS

List of Tables . . . . **vi**

List of Figures . . . . **vii**

List of Notations . . . . **ix**

Chapter 1
Introduction **1**
1.1 Structural Health Monitoring and Non-Destructive Evaluation 2
1.2 PZT and MFC Transducers 5
1.2.1 Piezoelectric Effect and PZT Actuator-Sensor 6
1.2.2 MFC Transducers 7
1.3 History of Non-Destructive Evaluation Using Guided Waves 8
1.3.1 Theory of Lamb Waves 8
1.4 Lamb Wave Inspection in Industries 9
1.5 Motivations and Objectives of the Research 10

Chapter 2
Lamb Wave in Plates **12**
2.1 Characteristic Equations 13
2.2 Dispersion Curves 15
2.3 Case study of Lamb wave propagation in an aluminum plate 16

Chapter 3
Analytical Calculation of Wave Propagation in Pipe-like Structures **20**
3.1 Derivation of Characteristic Equation 20
3.1.1 Mathematical Model 20
3.1.2 Governing Equation 21
3.1.3 Displacement Field 25
3.1.4 Stress Fields in Cylindrical Coordinate 25
3.1.5 Boundary Conditions 27
3.1.6 Residue Theorem 28

3.2 Dispersion Curves . . . 31
3.2.1 Name of Dispersion Curves . . . 31
3.2.2 Dispersion Curves for Pipes with Different Radius and Wall Thickness . . . 31
3.3 Analytical Solution . . . 33

Chapter 4
Numerical Simulation . . . 41
4.1 Finite Element Formulations . . . 41
4.2 Comparison of Numerical and Analytical Results . . . 43
4.3 Lamb Waves in Pipes with Defects . . . 46
4.4 Parametric Study of Responses for Different Defect Sizes . . . 48

Chapter 5
Summary and Conclusions . . . 53

Bibliography . . . 58

LIST OF TABLES

Table 2.1 Material Properties of the Steel Plate 16

Table 2.2 Material Properties of The Aluminum Plate 16

Table 3.1 Bessel functions in different regions [26] 24

LIST OF FIGURES

Figure 1.1 Possible areas to apply SHM systems: (a) the Golden Gate Bridge [21], and (b) an airplane [1]. (For interpretation of the references to color in this and all other figures, the reader is referred to the electronic version of this thesis.) 2

Figure 1.2 (a) Angular sweep with angle wedge, and (b) B-scan [13] 5

Figure 1.3 Schematics of PZT actuator. 6

Figure 1.4 Schematic of MFC transducer [33]. 7

Figure 1.5 (a) Cylindrical phased array [35] and (b) mathematical model for longitudinal wave propagation. 10

Figure 2.1 Schematic of Lamb wave in a plate. 13

Figure 2.2 Lamb wave modes in a plate. 14

Figure 2.3 Dispersion curves for (a) wavenumber; (b) phase velocity. 18

Figure 2.4 Input waveform 19

Figure 2.5 Comparison of experimental data and numerical simulation. 19

Figure 3.1 Contours for complex domain integration: (a) upper semicircle, and (b) lower semicircle 34

Figure 3.2 Different wave modes in a cylindrical system. 35

Figure 3.3 Dispersion curves for pipes of the outer radius $c_O = 136$ mm with the thicknesses (a) $t = 1$ mm and (b) $t = 2$ mm, (c) $t = 4$ mm and (d) $t = 6$ mm, respectively. 36

Figure 3.4 Dispersion curves of pipes of the thickness $t = 1$ mm with the outer radii (a) $c_O = 13$ mm and (b) $c_O = 25$ mm, (c) $c_O = 50$ mm and (d) $c_O = 136$ mm, respectively 37

Figure 3.5 Dispersion Curve of a pipe with $r_O = 136$ mm and $t = 1$ mm: (a) v_{ph} versus f and (b) ξ versus f. 38

Figure 3.6 (a) Tangential traction in time domain and (b) magnitudes of Fourier coefficients. 39

Figure 3.7 Displacements on the outer surface of a pipe with $c_O = 136$ mm and $t = 1$ mm: (a) u_z and (b) u_r on the outer surface. 40

Figure 4.1 (a) An example of discretized FE model, and (b) an element of the model. 45

Figure 4.2 Comparison of displacement field u_z on the outside surface of a pipe with c_O= 136 mm and t= 1 mm using mesh size in z direction of: (a) 1 mm, and (b) 0.25 mm. 47

Figure 4.3 Schematic of a pipe with a defect at z= 0.4 m. 48

Figure 4.4 Comparison of displacements measured in pipes (one is intact, and the other is damaged): Displacements u_z are measured (a) at z= 0.25 m, (b) at z= 0.45 m, and (c) at z= 0.6 m. 50

Figure 4.5 Comparison of displacements measured at $z = 0.6$ m on the outer surface of pipes with defect width of 1 mm vs 2 mm. 51

Figure 4.6 Comparison of displacements measured at $z = 0.35$ m on the outer surface of pipes with: (a) non-defect vs defect depth of 0.25 mm; (b) non-defect vs defect depth of 0.5 mm; (c) non-defect vs defect depth of 0.75 mm; (c) non-defect vs defect depth of 1 mm; (e) defect depth of 0.25 mm, 0.5 mm, 0.75 mm and 1 mm. 52

List of Notations

$\boldsymbol{\epsilon}$	Strain vector
$\mathbf{H}$	Vector potential function in a pipe
$\boldsymbol{B}$	Strain-displacement matrix
$\boldsymbol{H}_u$	Shape function
$\boldsymbol{K}$	Stiffness matrix
$\boldsymbol{M}$	Mass matrix
$\boldsymbol{u}$	Displacement vector
Δ	Determinant of dispersion equation
λ, μ	Lamé constants
∇	Three dimensional differential operator
ν	Poisson's ratio
ω	Angular frequency
ϕ	Scalar potential function
ψ	Vector potential function in a plate
ρ	Mass density
σ_{ij}	Stress component
ξ	Wavenumber
c_1	Longitudinal wave speed
c_2	Transverse wave speed
c_i	Inner radius of a pipe
c_o	Outer radius of a pipe
E	Young's modulus
f_i^B	Body force

h	Half of plate thickness
I_n, K_n	Modified Bessel functions
J_n	Bessel function of first kind
t	Time
u_r	Radial displacement
u_z	Axial displacement
v_{ph}	Phase velocity
x, y, z	Coordinates
Y_n	Bessel function of second kind

Chapter 1

Introduction

On August 1st, 2007, during the evening rush hour, I-35W Mississippi River Bridge collapsed suddenly, and killed 13 people. According to the report from National Transportation Safety Board [20], the disaster was caused by failure of the undersized gusset plate, which was not able to carry the increased concrete surface load. Back to history, hundreds of structural failures like I-35W Bridge collapse happened in the world, and most of them were caused by poor maintenance and lacking of inspection. On August 1st 1976, a road bridge with trams in Australia failed due to column fracture; On July 17th 1981, a double-deck suspended footbridge in Hyatte collapsed at Kansas City, Missouri because of overload and weak joints; On May 12th 2002, the Buran hangar in Kazakhstan collapsed due to structural failure caused by poor maintenance. All these disasters sounded an alarm that more attention is needed to be paid on the health states of the existing structures. Structural damages and failures threaten human lives and at the same time cause great financial losses. The United States spends a huge amount of money, more than 200 billion dollars per year, just for the maintenance of aircrafts, civil structures and mechanical engines. Structural Health Monitoring (SHM) emerges as an important engineering technique since it enables a cost-effective way to inspect structural health and provides basis for condition-based structural maintenance.

1.1 Structural Health Monitoring and Non-Destructive Evaluation

Before the review of structural health monitoring, it is important to introduce the definition of damage. In terms of structural health, damage is defined as the change introduced to the original system, which can cause adverse effects to its designed function or performance. All damages begin from the material level and grow to the components or the structure level when the structures undertake different kinds of loadings [34]. The adverse effects caused by damages might come immediately or in the future, and even a very small local damage may cause global collapse of the structures eventually, just as the collapse of I-35W Bridge. Therefore, our goal is to develop structural health monitoring systems which are sensitive to different kinds of damages, and it will enable us to avoid sudden failures of the structures by predicting the possible long term failures.

(a) (b)

Figure 1.1: Possible areas to apply SHM systems: (a) the Golden Gate Bridge [21], and (b) an airplane [1]. (For interpretation of the references to color in this and all other figures, the reader is referred to the electronic version of this thesis.)

Structure Health Monitoring refers to a wide rang of techniques, which include sensors, smart materials, data transmission, signal processing and analysis, and so on. It is an integrated process, which aims to diagnose damages, defects and flaws in structures by collecting data of structural responses under certain excitations or surrounding environments and analyzing those data. By conducting SHM, it is possible to determine the 'state' of the structural health and to predict the failure of the structures. There are five main objectives of SHM [25], which are defect detection and location, defect identification, defect assessment, defect monitoring, and failure prediction. On the other hand, SHM is usually conducted during the operation of the structures. It provides the real-time structural behavior under different excitations, which could be valuable information for better design and management of structures. Figure 1.1 shows the possible areas to apply SHM.

However, there are two main challenges in SHM techniques. One of the most significant challenges is signal interpretation. During the vibration-based SHM, the received signals are influenced not only by the damages in the structures, but also by the environmental conditions, the operational variabilities, and so on. Because of the complexity of the surrounding environments, diagnosis of the defects might be inaccurate. Another challenge is that SHM is often carried out by low frequency global vibration tests. This means typical local-based damages/defects might not be able to influence the result of the vibration test. Therefore, immediate structural collapse caused by local damages might not be predictable using the conventional techniques.

Non-Destructive Evaluation (NDE) is also developed to detect the flaws/faults in structures. One of the main difference between SHM and NDE is that in an SHM system, the locations of sensors, and the instrumentations are fixed from measurement to measurement, while in an NDE system the sensors and instrumentations are movable and the evaluation results of structures vary [9]. High flexibility makes NDE capable to be conducted at different locations of the structures and detect damages which might not be detected by SHM. Another difference between SHM and

NDE is that for NDE, evaluation of the remaining lifetime is usually not a goal of NDE.

Compared to SHM, NDE is conducted more locally and emphasizes more on the characteristics of the defects, such as orientation and size, or the severity of the damages [14]. There are mainly two types of NDE system, passive NDE and active NDE. The passive NDE systems use sensors to record the loads, stress in the structures and the influence of surrounding environments to the structures [17]. The passive NDE listens to the behavior of the structures under different load scenarios and environmental conditions. Active NDE uses transmitters to emit signals to the structures, and detects the presence and the characteristics of the damages by analyzing the responses given by the structures.

With the development of new materials and computational capacity, NDE techniques are rapidly developed in the past several decades. There are several major methodologies to conduct non-destructive evaluation. One of them is ultrasonic testing. For ultrasonic testing, transducers are applied to excite waves (vibrations) to propagate along the designed path. The signals passing through the materials or structures will be reflected when they meet the cracks, corrosions, or flaws in the materials, and received by the applied sensors. After that, the collected data will be analyzed to find out the locations and the sizes of the defects. Figure 1.2 shows the schematic of ultrasonic NDE.

Another commonly used method is performed by using dye penetrant. The method applies a penetrating liquid over the surface of the structure which needs to be detected. The liquid will enter to the discontinuities of cracks on the structures. The limitation of this method is that it is time consuming and usually used to detect surface flaws.

There is another non-destructive evaluation method called radiography method. It is used for most projects over a century. The industrial radiography uses an X-ray device as a source of

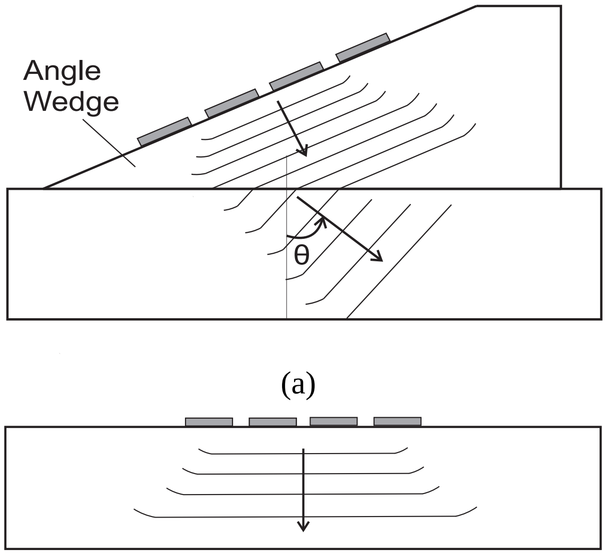

(a)

(b)

Figure 1.2: (a) Angular sweep with angle wedge, and (b) B-scan [13]

radiation. When the radiographic image taken by the X-ray device is processed, the image of varying density in the structure is obtained. By analyzing the image, the location and size of material imperfection can be identified.

In this thesis, we investigate NDE using Lamb waves in pipe-like structures. Lamb wave inspection is recently developed and utilized in non-destructive evaluation for plates and pipe-like structures due to its good performance in detecting the defects in thin-walled structures.

1.2 PZT and MFC Transducers

In order to excite Lamb waves in thin-walled structures, transducers are needed to be mounted on the surfaces of the structures and to emit different types of signals. In this section, we introduce two different transducers, which are the PZT actuator-sensor and the MFC transducer. The mechanisms of how they work are explained and their advantages and disadvantages are discussed.

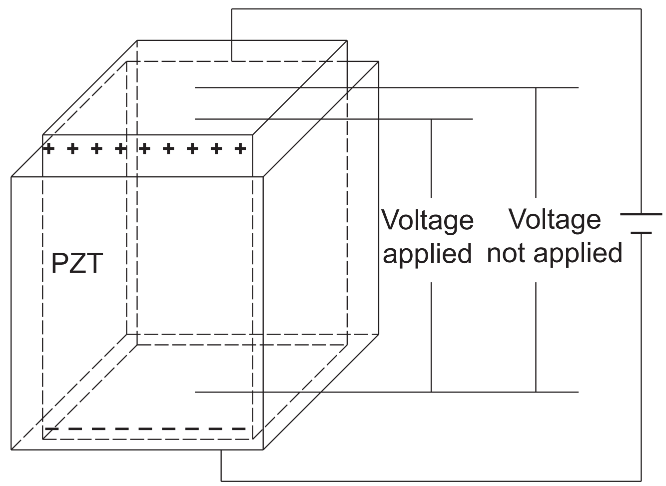

Figure 1.3: Schematics of PZT actuator.

1.2.1 Piezoelectric Effect and PZT Actuator-Sensor

PZT is the abbreviation of Piezoelectric ceramic Lead Zirconate Titanate. It uses the piezoelectric effect to measure the stress or strain in a structure by converting them to electrical charge or vice verse. Figure 1.3 shows the piezoelectric effect of a PZT sensor.

Piezoelectric effect is discovered by Pierre Curie in late nineteenth century, however its first application in sensing was 70 years later in 1950s. Within several decades, PZT has become one of the most commonly used piezoelectric materials because of its high piezoelectricity and sensitivity to stress and strain change. However, it is brittle and is not able to work in harsh environments for long time. Another disadvantage of PZT is that its flexibility is not good enough for curved surfaces such as surfaces of pipelines. Therefore, a more flexible actuator-sensor which can be perfectly mounted at the surface of pipe-like structures is developed.

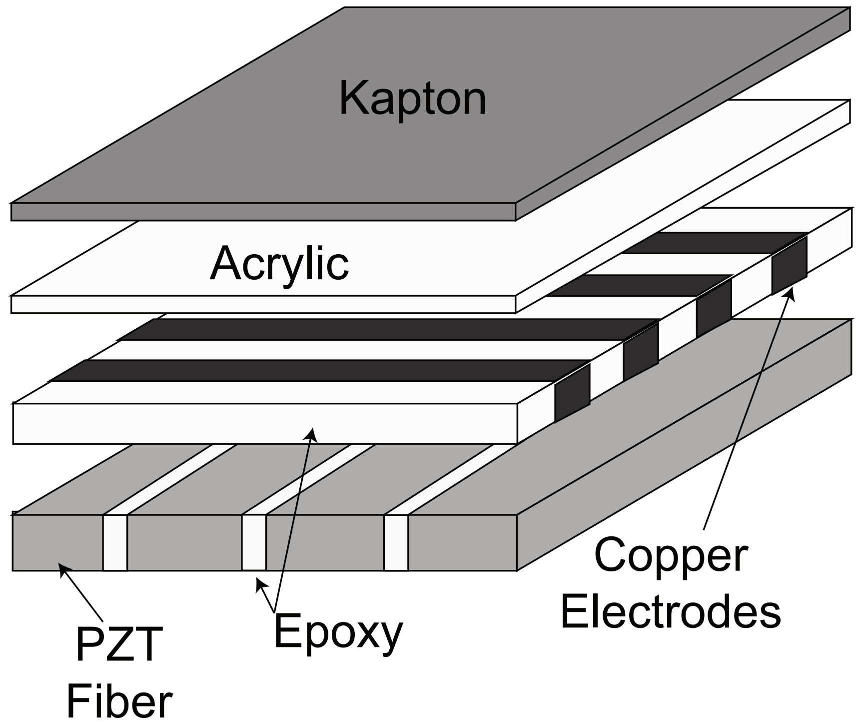

Figure 1.4: Schematic of MFC transducer [33].

1.2.2 MFC Transducers

The Macro-Fiber Composite (MFC) is an innovative, low-cost piezoelectric device developed by NASA in 1999 for controlling vibration and noise. The MFC is an actuator-sensor in the form of a thin patch. It consists of unidirectionally rectangular piezoceramic rods sandwiched between two layers of films, which containing tiny electrodes that can transfer a voltage directly to and from ribbon-shaped rods. Just like PZT, the MFC will stretch when it is subjected to a voltage. Figure 1.4 shows the schematic of the components of MFC. Compare to traditional piezoceramics, there are several advantages of MFC. Firstly, it is flexible and can be perfectly mounted at curved-shape structures, such as aircraft wings, pipelines, etc. Secondly, fine ceramic fibers provide higher strength and energy density over monolithic piezoceramics [27]. This makes MFC have higher durability to the harsh surrounding environments.

1.3 History of Non-Destructive Evaluation Using Guided Waves

Lamb waves, different from ultrasonic bulk waves, exist in free plates and pipes, and the Lamb wave particles move in two-dimensional vibration modes: the direction of wave propagation and the normal direction of the plate or pipe surface. Lamb waves propagate in plates of thickness less than 5λ, where λ is the Rayleigh wavelength [2]. When the plate thickness is greater than 5λ, the waves behave like Rayleigh waves, which are the surface waves existing on the boundary of a free half space.

1.3.1 Theory of Lamb Waves

Lamb waves are named after a British mathematician, Horace Lamb [22], to acknowledge his work on investigating the characteristics of vibration of a plate, the thickness of which is much smaller than the wavelength. His research demonstrated the difference between Lamb waves and bulk waves, and described the Lamb waves in mathematical equations. There are several reasons which make Lamb wave to be a relatively ideal tool to detect the defects in thin-walled waveguides. Firstly, Lamb waves can propagate for a longer distance than bulk waves. This makes lower cost non-destructive evaluation possible, since for longer pipelines fewer devices are needed for exciting and receiving Lamb wave signals. Secondly, Lamb waves are sensitive to defects in the waveguides. By selecting different wave modes, defects with different characteristics can be detected. Thirdly, due to the reflection by the boundaries, Lamb waves propagate through the thickness of the waveguides. It means Lamb wave inspection is able to detect defects not only on the surfaces of the waveguides but also inside the waveguides [7].

The propagation of guided waves has been studied for over a century. In 1889, Pochhammer and Chree [8] first investigated the wave propagation in a free infinite long cylindrical rod. At the same time, Lord Rayleigh [28] and Horace Lamb considered the problem of wave propagation in an elastic solid bounded by two parallel surfaces, the distance of which is much smaller than the wavelength. In the following few decades, theories of wave propagation in solid materials were fully developed by many researchers, such as Graff [18], Miklowitz [24], etc. Based on the theory developed by Pochhammer and Chree, Gazis [15] derived the characteristic equation of the guided waves propagating in a hollow isotropic cylinder, and calculated the solutions of the equation numerically [16]. Since then, dispersion curves of wave propagation in a hollow cylinder were developed, and the characteristics of guided wave modes were interpreted. After Gazis's work, a great deal of research has been conducted to investigate the wave motions in more complicated systems such as pipelines with multilayers [26], cylindrical structures surrounded by different environments [3, 31], and pipelines filled with flows.

1.4 Lamb Wave Inspection in Industries

Although the theoretical analysis of Lamb wave propagation in pipe-like structures has been well developed, there were few practical applications of guided waves for the inspection of pipes before 1990 due to the limitation of computational calculations [30]. From 2000, with rapid improvement of computational capacity, the techniques of guided wave inspection in pipelines were significantly improved, including transducer design and signal analysis. A typical NDE method used for pipe-like structures is shown in Figure 1.5 (a) [35]. A transmitter ring, which acts as a receiver as well, is mounted on a pipe, and different types of signals are emitted from the elements. Once Lamb waves are excited, the waves travel through the pipeline. When these waves meet defects in it, the waves change the modes and get reflected or diffracted. Therefore, the locations and sizes of defects can be diagnosed by analyzing the received signals. In this thesis, an analytical solution is developed based on the mathematical model as shown in Figure 1.5 (b), and the solution is compared with numerical results.

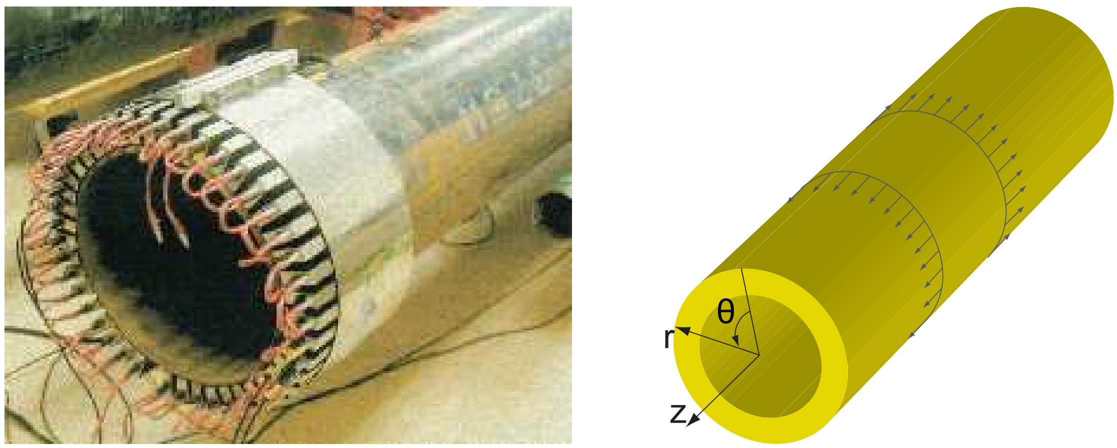

(a) (b)

Figure 1.5: (a) Cylindrical phased array [35] and (b) mathematical model for longitudinal wave propagation.

1.5 Motivations and Objectives of the Research

There are million miles of pipelines across the world, carrying important resources such as water, oil, gas, etc., and meanwhile they are exposed to harsh environments. Those pipelines are threatened by corrosion, weathering, or mechanical impact, which may cause the leakage of the transported materials. Therefore, it is urgently required to evaluate the integrity of the pipelines and ensure safe transportations of the resources.

As mentioned in the previous section, for thin-walled pipelines, the most commonly used non-destructive evaluation tool is Lamb wave. It overcomes the disadvantages of traditional ultrasonic testing, and the development of industrial techniques also accelerates the application of Lamb wave inspection.

In this thesis, our objectives are to:

- Study Lamb wave propagation in pipe-like structures both analytically and numerically;
- Compare the analytical and numerical results to verify the accuracy of numerical simulation;
- Simulate Lamb wave propagation in pipes with defects;
- Investigate the received signals by parametric study for different defect depths.

The calculated analytical solution is used as a reference signal to verify the accuracy of numerical simulation. On the other hand, once the accuracy of the numerical model is verified, it is used to simulate the wave behaviors in pipes with different sizes of defects, and provides a reference to track the development of the defects and investigate the influence of defect size on the received signals.

Chapter 2

Lamb Wave in Plates

A thin plate has two paralleled surfaces which form a guide to the Lamb waves and guide the direction of wave propagation in the plates. For practical application, the materials used in structures, such as steel and aluminum, have low damping inside the materials and the energy losses of the Lamb waves are very limited [12]. This is the reason for the long distance propagation of Lamb waves.

There are two basic types of wave modes existing in a plate, which are the symmetric modes S_i and the antisymmetric modes A_i, respectively. For symmetric wave modes, the particles vibrate symmetrically with respect to the mid-plane of the plate, while for antisymmetric modes, the wave modes are antisymmetric to the mid-plane of the plate. The schematics for the two modes are shown in Figure 2.2. The subscript i denotes the order of the wave mode, and it is assigned following the order of the cutoff frequency of each wave mode. As the frequency increases, the number of wave modes in a plate increases as well, thus it is possible that infinite number of wave modes might exit in a plate.

In order to utilize Lamb waves for plate inspection, a large amount of work has been done to investigate the characteristics of wave propagation analytically. In this chapter, the derivation of dispersion equations of Lamb wave propagation in plates is outlined. Detailed investigation of elastic wave propagation in solid materials can be found in many textbooks [4, 18, 32].

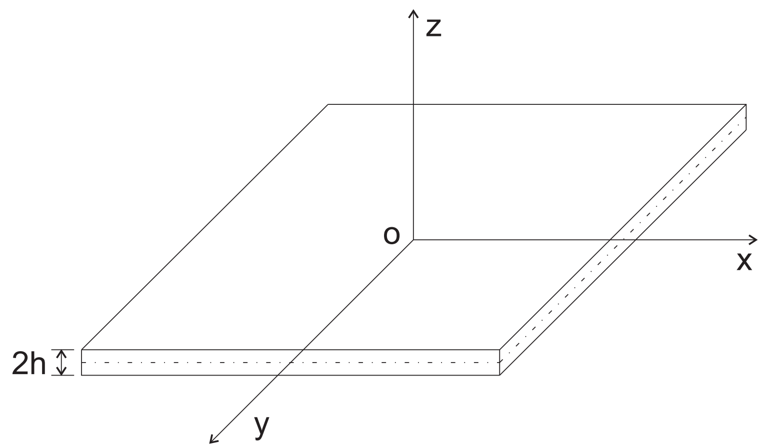

Figure 2.1: Schematic of Lamb wave in a plate.

A comprehensive solution of Lamb waves was developed by Mindlin in 1950, and Viktorov gave the detailed investigations of Lamb waves in plates, including dispersion curves and mode shapes in 1967 [37].

2.1 Characteristic Equations

The mathematical model of Lamb wave propagation in a plate is shown in Figure 2.1. Consider a plate with infinite extent in x and y directions, and thickness of $2h$. It is assumed that the plate is made of an isotropic material and is placed in vacuum. The wave equations [37] of longitudinal and shear Lamb wave are expressed as:

$$\begin{aligned} \frac{\partial^2\phi}{\partial x^2} + \frac{\partial^2\phi}{\partial z^2} + \frac{\omega^2}{c_1^2}\phi = 0 \\ \frac{\partial^2\psi}{\partial x^2} + \frac{\partial^2\psi}{\partial z^2} + \frac{\omega^2}{c_2^2}\psi = 0 \end{aligned} \tag{2.1}$$

where $c_1 = \sqrt{\frac{\lambda+2\mu}{\rho}}$, $c_2 = \sqrt{\mu/\rho}$ are the longitudinal and shear wave speeds respectively. Here, λ and μ are Lamé's constants, ρ is the mass density of the material. ϕ, ψ are the scalar and

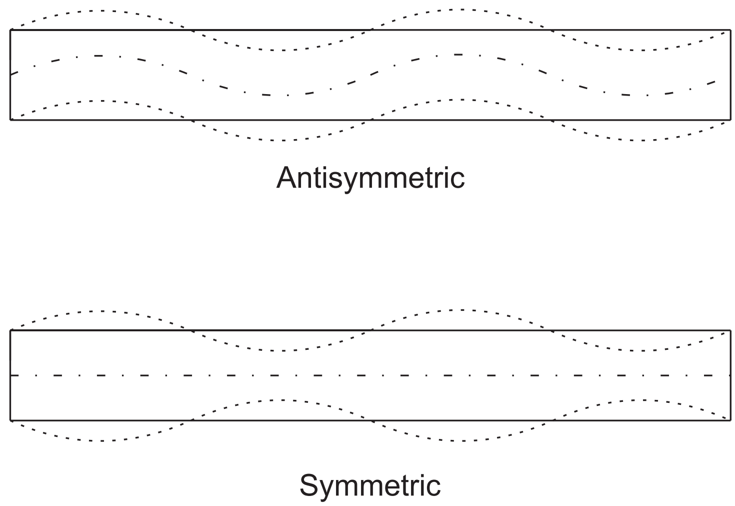

Figure 2.2: Lamb wave modes in a plate.

vector potential functions which are given as:

$$
\begin{aligned}
\phi &= [A_1 sin(pz) + A_2 cos(pz)]i(\xi x - \omega t), \\
\psi &= [B_1 sin(qz) + B_2 cos(qz)]e^{i(\xi x - \omega t)}.
\end{aligned}
\tag{2.2}
$$

where $p^2 = \omega^2/c_1^2 - \xi^2$, $q^2 = \omega^2/c_2^2 - \xi^2$. A_1, A_2, B_1 and B_2 are the unknown constants which are determined by boundary conditions, ω is the angular frequency, and ξ is the wavenumber.

For a free plate, by applying the boundary conditions that the components of stress fields are zero at $z = h$ and $z = -h$. The characteristic equations are obtained as:

$$
\begin{aligned}
\frac{\tan(qh)}{\tan(ph)} &= -\frac{4\xi^2 qp}{(\xi^2 - q^2)^2} \\
\frac{\tan(qh)}{\tan(ph)} &= -\frac{(\xi^2 - q^2)^2}{4\xi^2 qp}
\end{aligned}
\tag{2.3}
$$

Eq. (2.3) are for symmetric and anti-symmetric wave modes, respectively.

2.2 Dispersion Curves

Although Lamb waves have unparalleled advantages in long distance structural inspection, signal interpretation is a major issue which makes the development of the application of Lamb wave inspection much slower than its theory. As discussed above, with high frequency excitation, a large number of Lamb wave modes exist in a plate. Those modes are of different amplitudes and phase velocities and this make it difficult to distinguish the incident signals and the signals reflected/refracted by the defects. On the other hand, Lamb waves are dispersive when they travel through the waveguides. It means that when the distance the wave traveling is larger, the amplitudes of the wave modes decreases, which also increases the difficulty to find the flaws in the structures. Therefore, one of the goals is to limit the number of wave modes in the plate and find a wave mode which is suitable for the inspection.

Dispersion curves contain the information of the characteristics of each wave mode and thus is important for selecting proper wave modes for damage detection. In order to calculate the dispersion curves in a certain plate, the material properties are chosen as shown in Table 2.1. Figure 2.3 shows the dispersion curves for a plate of 1 mm thickness. It is generated by a free software PACshare DispersionPlus Curves (Physical Acoustics Corporation, Princeton Junction, NJ, USA) [10]. From Figure 2.3, we can see two different ways to present dispersion curves. Figure 2.3 (a) shows the dispersion curves in wavenumber projection. Wavenumber projection comes from the solutions of dispersion equations, showing the possible wave modes in the wave guide. Compared to dispersion curves displayed in phase velocity, the wavenumber dispersion curves have higher linearity and are selected because of easier calculation. Another common way to display dispersion curves is in the form of phase velocity as shown in Figure 2.3 (b). Phase

Table 2.1: Material Properties of the Steel Plate

Young's Modulus (GPa)	Poisson's Ratio	Mass Density (Kg/m^3)
206	0.3	7850

Table 2.2: Material Properties of The Aluminum Plate

Young's Modulus (GPa)	Poisson's Ratio	Mass Density (Kg/m^3)
70	0.33	2700

velocity is the velocity at which the phase/crest travels. The relationship between phase velocity and wavenumber is $v_{ph} = 2\pi f/\xi$. Actually, Figure 2.3 (b) is most commonly used since it is easy to read the characteristics of each wave mode.

From Figure 2.3 (b), we can see that for the plate of 1 mm thickness there are two wave modes existing under frequency of 1 MHz: the S_0 and A_0 modes. S_0 is the fundamental wave mode, which has almost constant phase velocity through out the frequency range. Because of the stability of S_0, it is usually selected as an relatively ideal mode for non-destructive evaluation in plates.

2.3 Case study of Lamb wave propagation in an aluminum plate

In this section, finite element simulation is employed to study the Lamb wave behavior in an aluminum plate using FEAP [36], and the results are compared with published experimental data provided by D. W. Greve, *et al* [19]. The material properties of the aluminum plate are shown in Table 2.2.

In the experiment, two PZT transducers are attached to the aluminum plate by silver epoxy. The thickness of the plate is 1.59 mm, and the distance between the transducers is 20 cm. By applying voltage on the PZT transducers, shear force is introduced to the plate due to the piezoelectric effect. Based on the experiment, a numerical model is created, and the geometry of which is set to be 0.8 m in x-direction, 0.5 m in y-direction and 1.59 mm in z-direction. The mesh sizes in x, y, and z directions are 1 mm, 1 mm and 0.795 mm, respectively. To simplify the numerical model, a point shear force is applied at $x = 0.3$ m, and the signals are measured at $x = 0.5$ m, which is 20 cm away from the excitation. The shape of excitation is shown in Figure 2.4. It is given by a windowed sinusoidal signal expressed as:

$$V(t) = \begin{cases} V_0 \sin(\omega t) \left(\frac{\sin(\omega t)}{10} \right)^2 & t < \frac{10\pi}{\omega} \\ 0 & \text{otherwise} \end{cases} \tag{2.4}$$

Comparison is conducted between the numerical and the experimental results to verify the accuracy of the finite element model. Figure 2.5 shows the comparison between the two results. From the figure, we observe that, S_0 mode travels faster than the A_0 mode. In addition, slight differences in arrival time are observed for both S_0 and A_0 modes in the comparison. It is noticed that the magnitude of the A_0 mode is much larger than that obtained from the experimental study.

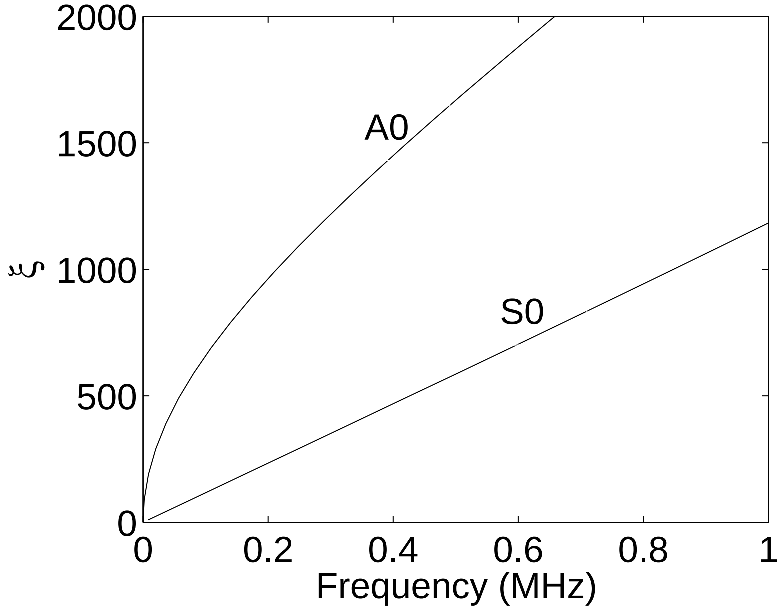

(a)

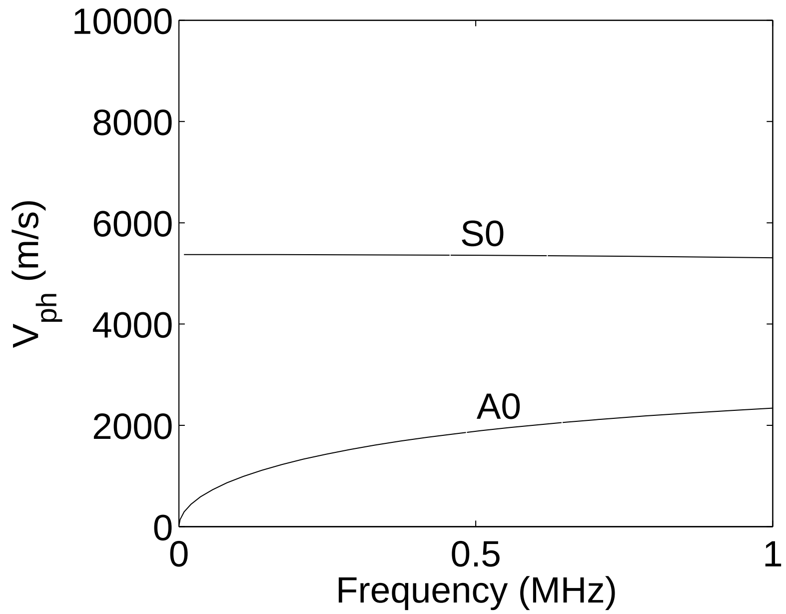

(b)

Figure 2.3: Dispersion curves for (a) wavenumber; (b) phase velocity.

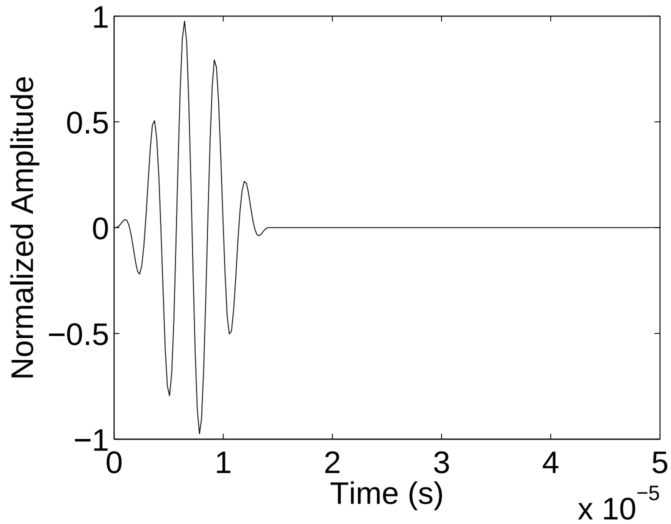

Figure 2.4: Input waveform

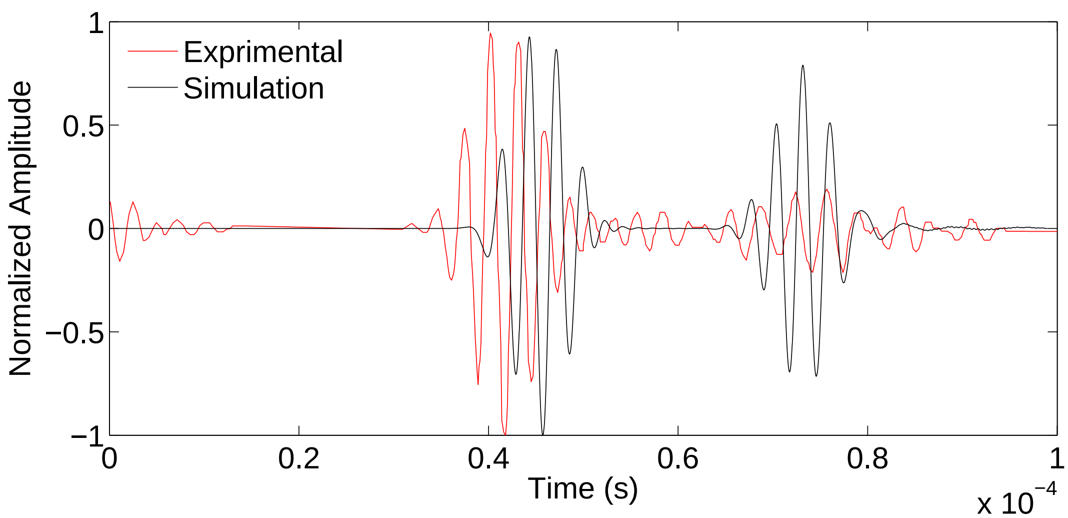

Figure 2.5: Comparison of experimental data and numerical simulation.

Chapter 3

Analytical Calculation of Wave Propagation in Pipe-like Structures

In this section, the characteristic equation of Lamb wave propagating in the pipe shown in Figure 1.5 (b) is derived. The characteristic equation, also called dispersion equation, is obtained from finding the possible wave modes in a given wave guide [29]. The dispersion curves contain information of the geometry, the material properties of the waveguide, and the frequency of the input excitation. At a specific frequency, solutions of the characteristic equation might be obtained numerically, and each solution corresponds to the wave speed of each wave mode. By tracking the frequency, solutions can be plotted as continuous curves which are called the dispersion curves. From the dispersion curves, the fundamental modes for a configuration might be estimated, and the corresponding wave velocities can be calculated.

3.1 Derivation of Characteristic Equation

3.1.1 Mathematical Model

Figure 1.5 (b) shows the mathematical model of the problem to be solved. An infinite hollow cylinder of a single layer made of an isotropic material is placed in vacuum. The shear traction is applied on the circumference of the pipe at z-coordinates l and $-l$. The inside and outside radii of the pipe are denoted as c_i and c_O, respectively. For the surface excitation, the Morlet wavelet which contains a wide range of frequencies, is given as the input tangential traction. The steady state solution for a sinusoidal excitation is obtained, and is utilized to express the transient solution by the wide-band excitation.

3.1.2 Governing Equation

The governing equation of wave propagation in an isotropic material, known as Navier's displacement equation of motion, is written as [27]

$$(\lambda + 2\mu)\nabla\nabla \cdot \mathbf{u} + \mu\nabla^2\mathbf{u} = \rho(\frac{\partial^2 \mathbf{u}}{\partial t^2}), \tag{3.1}$$

where λ and μ are Lamé constants of the material, ρ is the mass density, $\boldsymbol{u}$ is the displacement vector, and ∇ is the three dimensional differential operator. Using Helmholtz decomposition, we can express the displacement fields in terms of the scalar potential ϕ and the vector potential $\boldsymbol{H}$ as

$$\mathbf{u} = \nabla\phi + \nabla \times \mathbf{H}. \tag{3.2}$$

Substituting Eq. (3.2) into Eq. (3.1), we have

$$\nabla[(\lambda + 2\mu)\nabla^2\phi - \rho\frac{\partial^2 \phi}{\partial t^2}] + \nabla \times [\mu\nabla^2\mathbf{H} - \rho\frac{\partial^2 \mathbf{H}}{\partial t^2}] = 0. \tag{3.3}$$

To satisfy Eq. (3.3) in any condition, we have

$$
\begin{aligned}
c_1^2\nabla^2\phi &= \frac{\partial^2\phi}{\partial t^2},\\
c_2^2\nabla^2\mathbf{H} &= \frac{\partial^2\mathbf{H}}{\partial t^2},
\end{aligned}
\tag{3.4}
$$

where $\mathbf{H}$ consists of H_r, H_θ and H_z, and the longitudinal velocity c_1 and the shear velocity c_2 are given, respectively as

$$
c_1 = \sqrt{\frac{\lambda + 2\mu}{\rho}} \qquad c_2 = \sqrt{\frac{\mu}{\rho}}. \tag{3.5}
$$

Rewriting Gazis's [15] potential field in exponential forms, we have

$$
\begin{aligned}
\phi &= f(r)cos(n\theta)e^{i(\xi z-\omega t)},\\
H_r &= g_r(r)sin(n\theta)e^{i(\xi z-\omega t)},\\
H_\theta &= g_\theta(r)cos(n\theta)e^{i(\xi z-\omega t)},\\
H_z &= g_r(r)sin(n\theta)e^{i(\xi z-\omega t)},
\end{aligned}
\tag{3.6}
$$

where ω is the radial frequency, ξ is the wave number, n indicates the number of waves in the circumferential direction. It should be noted that the applied shear traction excites waves that propagate only along the axial direction of the pipe. Therefore, $n = 0$, and H_r and H_z are zeros as well. The Laplacian operator ∇^2 for scalar potential ϕ can be expressed in the cylindrical coordinate system as

$$
\nabla^2\phi = \frac{\partial^2\phi}{\partial r^2} + \frac{1}{r}\frac{\partial\phi}{\partial r} + \frac{\partial^2\phi}{\partial z^2}, \tag{3.7}
$$

while for the vector potential $\mathbf{H}$, the Laplacian operator can be rewritten as:

$$
\nabla^2\mathbf{H} = \nabla\cdot(\nabla\mathbf{H}), \tag{3.8}
$$

where the gradient of $\mathbf{H}$, $\nabla\mathbf{H}$ is expressed as:

$$\begin{aligned}\nabla\mathbf{H} &= \frac{\partial H_r}{\partial r}e_r\otimes e_r+\frac{1}{r}(\frac{\partial H_r}{\partial\theta}-H_\theta)e_r\otimes e_\theta+\frac{\partial H_r}{\partial z}e_r\otimes e_z\\ &+\frac{\partial H_\theta}{\partial r}e_\theta\otimes e_r+\frac{1}{r}(\frac{\partial H_\theta}{\partial\theta}+H_r)e_\theta\otimes e_\theta+\frac{\partial H_\theta}{\partial z}e_\theta\otimes e_z\\ &+\frac{\partial H_z}{\partial r}e_z\otimes e_r+\frac{1}{r}\frac{\partial H_z}{\partial\theta}e_z\otimes e_\theta+\frac{\partial H_z}{\partial z}e_z\otimes e_z.\end{aligned}\tag{3.9}$$

Denote Eq. (3.10) in matrix form as:

$$\mathbf{S}=\begin{bmatrix}\frac{\partial H_r}{\partial r} & \frac{1}{r}(\frac{\partial H_r}{\partial\theta}-H_\theta) & \frac{\partial H_r}{\partial z}\\ \frac{\partial H_\theta}{\partial r} & \frac{1}{r}(\frac{\partial H_\theta}{\partial\theta}+H_r) & \frac{\partial H_\theta}{\partial z}\\ \frac{\partial H_z}{\partial r} & \frac{1}{r}\frac{\partial H_z}{\partial\theta} & \frac{\partial H_z}{\partial z}\end{bmatrix}\tag{3.10}$$

Here $\mathbf{S}$ is a second-order tensor. Divergence of $\mathbf{S}$ can be obtained as:

$$\begin{aligned}\nabla\cdot\mathbf{S} &= \left\{\frac{\partial S_{rr}}{\partial r}+\frac{1}{r}[\frac{\partial S_{r\theta}}{\partial\theta}+(S_{rr}-S_{\theta\theta})]+\frac{\partial S_{r\theta}}{\partial z}\right\}e_r\\ &+\left\{\frac{\partial S_{\theta r}}{\partial r}+\frac{1}{r}[\frac{\partial S_{\theta\theta}}{\partial\theta}+(S_{\theta r}+S_{r\theta})]+\frac{\partial S_{\theta z}}{\partial z}\right\}e_\theta\\ &+\left\{\frac{\partial S_{zr}}{\partial r}+\frac{1}{r}[\frac{\partial S_{z\theta}}{\partial\theta}+S_{zr}]+\frac{\partial S_{zz}}{\partial z}\right\}e_z.\end{aligned}\tag{3.11}$$

Since in our case, only longitudinal wave modes are considered, Eq. (3.12) in circumference direction can be obtained as:

$$\nabla^2 H_\theta=\frac{\partial^2 H_\theta}{\partial r^2}+\frac{1}{r}\frac{\partial H_\theta}{\partial r}+\frac{\partial^2 H_\theta}{\partial z^2}-\frac{H_\theta}{r^2}.\tag{3.12}$$

Table 3.1: Bessel functions in different regions [26]

when $\xi < \frac{\omega}{c_1}$	when $\frac{\omega}{c_1} < \xi < \frac{\omega}{c_2}$	when $\xi > \frac{\omega}{c_2}$
$\alpha_1 = \sqrt{\alpha^2}; \beta_1 = \sqrt{\beta^2}$	$\alpha_1 = \sqrt{-\alpha^2}; \beta_1 = \sqrt{\beta^2}$	$\alpha_1 = \sqrt{-\alpha^2}; \beta_1 = \sqrt{-\beta^2}$
$\gamma_1 = 1; \gamma_2 = 1$	$\gamma_1 = -1; \gamma_2 = 1$	$\gamma_1 = -1; \gamma_2 = -1$
$Z_n(\alpha r) = J_n(\alpha r)$	$Z_n(\alpha r) = I_n(\alpha r)$	$Z_n(\alpha r) = I_n(\alpha r)$
$W_n(\alpha r) = Y_n(\alpha r)$	$W_n(\alpha r) = K_n(\alpha r)$	$W_n(\alpha r) = K_n(\alpha r)$
$Z_n(\beta r) = J_n(\beta r)$	$Z_n(\beta r) = J_n(\beta r)$	$Z_n(\beta r) = I_n(\beta r)$
$W_n(\beta r) = Y_n(\beta r)$	$W_n(\beta r) = Y_n(\beta r)$	$W_n(\beta r) = K_n(\beta r)$

To simplify the derivation, the spatial Fourier transform along z-direction is applied to Eq. (3.4). With the property of Fourier transform $\frac{\partial \hat{f}}{\partial x} = i\xi \hat{f}$, Eq. (3.4) can be written as

$$\begin{aligned} \frac{\partial^2 \hat{\phi}}{\partial r^2} + \frac{1}{r}\frac{\partial \hat{\phi}}{\partial r} + \left(\frac{\omega^2}{c_1^2} - \xi^2\right)\hat{\phi} = 0, \\ \frac{\partial^2 \hat{H}_\theta}{\partial r^2} + \frac{1}{r}\frac{\partial \hat{H}_\theta}{\partial r} + \left(\frac{\omega^2}{c_2^2} - \xi^2 - \frac{1}{r^2}\right)\hat{\phi} = 0. \end{aligned} \tag{3.13}$$

The general solutions of Eq. (3.13) are

$$\begin{aligned} \hat{\phi} = [AZ_0(\alpha r) + BW_0(\alpha r)]e^{-i\omega t}, \\ \hat{H}_\theta = [CZ_1(\beta r) + DW_1(\beta r)]e^{-i\omega t}. \end{aligned} \tag{3.14}$$

where $\alpha^2 = \omega^2/c_1^2 - \xi^2$, $\beta^2 = \omega^2/c_2^2 - \xi^2$, the notations Z_0, Z_1, W_0 and W_1 are four different types of Bessel functions. Table 3.1 shows how to choose appropriate parameters and Bessel functions to make the solution stable. In Table 3.1, J_n and Y_n are the Bessel functions of the first kind and the second kind, respectively, and I_n, K_n are the modified Bessel functions.

3.1.3 Displacement Field

With only longitudinal modes excited, the displacement fields can be obtained as

$$\begin{aligned} u_r &= \frac{\partial \phi}{\partial r} - \frac{\partial H_\theta}{\partial z}, \\ u_z &= \frac{\partial \phi}{\partial z} + \frac{1}{r}\frac{\partial (H_\theta r)}{\partial r}. \end{aligned} \tag{3.15}$$

Taking the Fourier transform of Eq. (3.15) and substituting Eq. (3.14), we have

$$\begin{aligned} \hat{u}_r &= -\gamma_1 \alpha_1 Z_1(\alpha_1 r)A - \alpha_1 W_1(\alpha_1 r)B - i\xi Z_1(\beta_1 r)C - i\xi W_1(\beta_1 r)D, \\ \hat{u}_z &= i\xi Z_0(\alpha_1 r)A + i\xi W_0(\alpha_1 r)B + \beta_1 Z_0(\beta_1 r)C + \gamma_2 \beta_1 W_0(\beta_1 r)D. \end{aligned} \tag{3.16}$$

Here, the term $e^{-i\omega t}$ is omitted for simplicity, and it will be brought back in the final expressions of u_r and u_z.

3.1.4 Stress Fields in Cylindrical Coordinate

The relationships between strains and displacements are expressed as

$$\begin{aligned} \epsilon_{rr} &= \frac{\partial u_r}{\partial r}, \\ \epsilon_{rz} &= \frac{1}{2}(\frac{\partial u_r}{\partial z} + \frac{\partial u_z}{\partial r}), \end{aligned} \tag{3.17}$$

and the stress-strain relations are given by Hooke's Law as

$$\begin{aligned} \sigma_{rr} &= \lambda \nabla^2 \phi + 2\mu \epsilon_{rr}, \\ \sigma_{rz} &= 2\mu \epsilon_{rz}. \end{aligned} \tag{3.18}$$

Stress fields σ_{rr} and σ_{rz} are obtained by substituting Eq. (3.17) to Eq. (3.18) as

$$\begin{aligned}\sigma_{rr} &= (\lambda + 2\mu)(\frac{\partial u_r}{\partial r}) + \frac{\lambda}{r}u_r + \lambda\frac{\partial u_z}{\partial z},\\ \sigma_{rz} &= \mu(\frac{\partial u_r}{\partial z} + \frac{\partial u_z}{\partial r}).\end{aligned} \tag{3.19}$$

By taking the Fourier transform of Eq. (3.19) and substituting Eq. (3.16) to Eq. (3.19), the terms $\hat{\sigma}_{rr}$ and $\hat{\sigma}_{rz}$ are written as

$$\begin{aligned}\hat{\sigma}_{rr} = {} & [(\xi^2 - \beta^2)Z_0(\alpha_1 r) + \gamma_1\frac{2\mu\alpha_1}{r}Z_1(\alpha_1 r)]A + [(\xi^2 - \beta^2)W_0(\alpha_1 r) + \frac{2\mu\alpha_1}{r}W_1(\alpha_1 r)]B\\ & + 2\mu[-i\xi\beta_1 Z_0(\beta_1 r) + \frac{i\xi}{r}Z_1(\beta_1 r)]C + 2\mu[-i\gamma_2\xi\beta_1 W_0(\beta_1 r) + \frac{i\xi}{r}W_1(\beta_1 r)]D,\\ \hat{\sigma}_{rz} = {} & -2i\gamma_1\xi\mu\alpha_1 Z_1(\alpha_1 r)A - 2i\xi\mu\alpha_1 W_1(\alpha_1 r)B + \mu(\xi^2 - \beta^2)Z_1(\beta_1 r)C\\ & + \mu(\xi^2 - \beta^2)W_1(\beta_1 r)D.\end{aligned} \tag{3.20}$$

3.1.5 Boundary Conditions

As shown in Figure 1.5 (b), a set of shear traction is applied at the coordinates $z = l$ and $z = -l$ on the outer surface of the pipeline. The boundary conditions can be expressed as

$$\begin{aligned} &\sigma_{rr}(r = c_o) = 0, \\ &\sigma_{rz}(r = c_o) = [\delta(z - l) - \delta(z + l)]e^{-i\omega t}, \\ &\sigma_{rr}(r = c_i) = 0, \\ &\sigma_{rz}(r = c_i) = 0. \end{aligned} \tag{3.21}$$

By replacing r in Eq. (3.20) with c_o and c_i, respectively, and by applying Fourier transform to the boundary condition [27], we obtain

$$\mathbf{M}\begin{bmatrix} A \\ B \\ C \\ D \end{bmatrix} = \begin{bmatrix} m_{11} & m_{12} & m_{13} & m_{14} \\ m_{21} & m_{22} & m_{23} & m_{24} \\ m_{31} & m_{32} & m_{33} & m_{34} \\ m_{41} & m_{42} & m_{43} & m_{44} \end{bmatrix}\begin{bmatrix} A \\ B \\ C \\ D \end{bmatrix} = -2isin(\xi l)\begin{bmatrix} 0 \\ 1 \\ 0 \\ 0 \end{bmatrix}, \tag{3.22}$$

where $\mathbf{M}$ is the coefficient matrix, and the components are written as

$$\begin{aligned} m_{11} &= (\xi^2 - \beta^2)Z_0(\alpha_1 c_o) + \gamma_1 \frac{2\mu\alpha_1}{c_o} Z_1(\alpha_1 c_o), & m_{21} &= -2i\gamma_1\xi\mu\alpha_1 Z_1(\alpha_1 c_o), \\ m_{12} &= (\xi^2 - \beta^2)W_0(\alpha_1 C_o) + \frac{2\mu\alpha_1}{c_o} W_1(\alpha_1 c_o), & m_{22} &= -2i\xi\mu\alpha_1 W_1(\alpha_1 c_o), \\ m_{13} &= 2\mu[-i\xi\beta_1 Z_0(\beta_1 r) + \frac{i\xi}{c_o} Z_1(\beta_1 c_o)], & m_{23} &= \mu(\xi^2 - \beta^2)Z_1(\beta_1 c_o), \\ m_{14} &= 2\mu[-i\gamma_2\xi\beta_1 W_0(\beta_1 c_o) + \frac{i\xi}{c_o} W_1(\beta_1 c_o)], & m_{24} &= \mu(\xi^2 - \beta^2)W_1(\beta_1 c_o). \end{aligned} \tag{3.23}$$

The expressions of m_{31} to m_{44} in the matrix $\mathbf{M}$ can be obtained by replacing c_o with c_i. Then, the constants A, B, C, and D might be solved by applying Cramer's rule as

$$A = \frac{a}{\Delta(\xi)}, \qquad B = \frac{b}{\Delta(\xi)}, \qquad C = \frac{c}{\Delta(\xi)}, \qquad D = \frac{d}{\Delta(\xi)}, \tag{3.24}$$

where

$$a = -i2sin(\xi l)\det \begin{bmatrix} 0 & m_{12} & m_{13} & m_{14} \\ 1 & m_{22} & m_{23} & m_{24} \\ 0 & m_{32} & m_{33} & m_{34} \\ 0 & m_{42} & m_{43} & m_{43} \end{bmatrix}, \qquad \Delta = \det(\mathbf{M}). \tag{3.25}$$

Similarly, the expressions for b, c and d might be obtained by substituting $[0\ 1\ 0\ 0]^T$ to the second column, third column, and fourth column of $\mathbf{M}$, respectively. Here, the dispersion equation is written as $\Delta = 0$.

3.1.6 Residue Theorem

Once the constants A, B, C and D in Eq. (3.22) are calculated, the displacement fields u_{rr} and u_{rz} might be obtained by applying inverse Fourier transform to Eq. (3.16) as

$$\begin{aligned} u_r = \frac{1}{2\pi}\int_{-\infty}^{+\infty} \frac{e^{i(\xi z - \omega t)}}{\Delta(\xi)}[-\gamma_1\alpha_1 a(\xi)Z_1(\alpha_1 r) - \alpha_1 b(\xi)W_1(\alpha_1 r) \\ - i\xi c(\xi)Z_1(\beta_1 r) - i\xi d(\xi)W_1(\beta_1 r)]d\xi, \\ u_z = \frac{1}{2\pi}\int_{-\infty}^{+\infty} \frac{e^{i(\xi z - \omega t)}}{\Delta(\xi)}[i\xi a(\xi)Z_0(\alpha_1 r) + i\xi b(\xi)W_0(\alpha_1 r) \\ + \beta_1 c(\xi)Z_0(\beta_1 r) + \gamma_2\beta_1 d(\xi)W_0(\beta_1 r)]d\xi. \end{aligned} \tag{3.26}$$

The next step is to evaluate the integration above by carrying out residue theorem. Residue theorem [23] is one of the most important tool employed in general wave propagation problems [18]. It is effective to calculate the line integrals of analytical functions in complex domain, and has been utilized popularly to obtain analytical solutions for various kinds of waves.

Before applying residue theorem, we rewrite Eq. (3.26) as:

$$\begin{aligned} u_r &= \frac{1}{2\pi}\int\limits_{-\infty}^{+\infty}\frac{e^{i(\xi z-\omega t)}}{\Delta(\xi)}f(\xi)d\xi, \\ u_z &= \frac{1}{2\pi}\int\limits_{-\infty}^{+\infty}\frac{e^{i(\xi z-\omega t)}}{\Delta(\xi)}g(\xi)d\xi. \end{aligned} \tag{3.27}$$

Since the two expressions in Eq. (3.27) are similar, we use the expression of u_r to show the application of residue theorem. Rewrite u_r as:

$$\frac{1}{2\pi}\int\limits_{-\infty}^{+\infty}\frac{e^{i(\xi z-\omega t)}}{\Delta(\xi)}f(\xi)d\xi = \frac{1}{2\pi}\int_C\frac{e^{i(\xi z-\omega t)}}{\Delta(\xi)}f(\xi)d\xi - \frac{1}{2\pi}\int_{C'}\frac{e^{i(\xi z-\omega t)}}{\Delta(\xi)}f(\xi)d\xi \tag{3.28}$$

where C is the closed contour in the complex plane, and C' is the semicircle of C. There are two main aspects we need to consider in applying residue theorem. The first issue is to select the closed contour in the complex plane, which could be the upper or lower contour as shown in Figure 3.1.

Choose the upper closed contour for example, let $\xi = Re^{i\theta}$, and denote the integration along the semicircle C' as I. Then, I can be expressed as:

$$I = \lim_{R\to\infty}\int\limits_0^{\pi}\frac{f(Re^{i\theta})e^{i(Rzcos\theta-\omega t)}e^{-Rzsin\theta}}{\Delta(Re^{i\theta})}iRe^{i\theta}d\theta, \tag{3.29}$$

The important term in Eq. (3.29) is $e^{-Rz\sin\theta}$. In our problem, we are interested in the displacement fields at $z > a$. From Eq. (3.29), it is easy to find that in order to make the integration along the semicircle to be zero, $\sin\theta$ is required to be positive. Therefore, we select the upper side closed contour to evaluate the integration.

The second issue we need to consider is the poles located on the real axial of the complex plane. Based on the previous description of the integration on the semicircle C', rewrite Eq. (3.28) in the form of residues, we have:

$$\int_{-\infty}^{+\infty} \frac{e^{i(\xi z-\omega t)}}{\Delta(\xi)} f(\xi) d\xi = 2\pi i \sum Res, \tag{3.30}$$

where the residues are expressed as:

$$Res = \frac{e^{i(\hat{\xi} z-\omega t)}}{\Delta'(\hat{\xi})} f(\hat{\xi}), \tag{3.31}$$

Due to the physical meaning of the wave number, ξ's are set to be positive. Therefore, we excluded the negative poles and have the outward propagating waves in the form of $e^{i(\hat{\xi}z-\omega t)}$. Similarly, we evaluate the integration of u_z. Finally, the expressions of u_r, u_z are given as

$$\begin{aligned}
u_r &= \sum_{\hat{\xi}} \frac{ie^{i(\hat{\xi}z-\omega t)}}{\Delta'(\hat{\xi})}[-\gamma_1\alpha_1 a(\hat{\xi})Z_1(\alpha_1 r) - \alpha_1 b(\hat{\xi})W_1(\alpha_1 r) - i\hat{\xi}c(\hat{\xi})Z_1(\beta_1 r) - i\hat{\xi}d(\hat{\xi})W_1(\beta_1 r)], \\
u_z &= \sum_{\hat{\xi}} \frac{ie^{i(\hat{\xi}z-\omega t)}}{\Delta'(\hat{\xi})}[i\xi a(\hat{\xi})Z_0(\alpha_1 r) + i\hat{\xi}b(\hat{\xi})W_0(\alpha_1 r) + \beta_1 c(\hat{\xi})Z_0(\beta_1 r) + \gamma_2\beta_1 d(\hat{\xi})W_0(\beta_1 r)],
\end{aligned} \tag{3.32}$$

where $\hat{\xi}$ is the solution of the dispersion equation, and Eq. (3.32) describes the response under a steady state excitation. To get the response under a transient excitation, it is required to apply Fast Fourier Transform (FFT) [6] to decompose the input signal into a set of sinusoidal inputs with different frequencies and amplitudes, and then superpose the calculated displacement by each input to get the final response.

3.2 Dispersion Curves

3.2.1 Name of Dispersion Curves

There are three types of modes in a cylindrical system, which are the longitudinal (L), the flexural (F) and the torsional (T) modes. Figure 3.2 shows the three types of modes. For each mode type, a two index system, e.g. L (M,N), is used to indicate the wave modes. The first integer M denotes the circumferential order of the mode, while the second integer N is the counter value [26]. The modes spanning from zero frequency are named as the first mode, and the others are given the names consequently in the order of their cutoff frequency. All the longitudinal modes of circumferential order $M = 0$ are axisymmetic.

3.2.2 Dispersion Curves for Pipes with Different Radius and Wall Thickness

In the previous section, we have obtained the expression of the dispersion equation $\Delta = 0$. By numerical calculations, the solutions of the equation might be plotted. To obtain the solutions of the dispersion equation, we fix the frequency and search the wave numbers that satisfy $\det(\boldsymbol{M}) = 0$. Due to the nature of Bessel functions, the determinant of $\boldsymbol{M}$ is sensitive to the wavenumber. Therefore, it is not trivial to find the wavenumbers to make the determinant to vanish. In this thesis, the wavenumber step is set to be $\Delta\xi = 0.3$ to calculate the determinants of the coefficient matrix $\boldsymbol{M}$. Then, the linear interpolation technique is used to obtain zeros when the determinants change the sign.

Figure 3.3 shows the dispersion curves for pipes that have the outer radius of 136 mm with the wall thicknesses of 1 mm, 2 mm, 4 mm and 6 mm, respectively. It is observed that dispersion curves are sensitive to the geometry of the pipe. More wave modes exist under a certain frequency if the thickness is larger. Another important observation is that the dispersion curves show the dispersion of velocity versus frequency. In NDE techniques, excitation signals usually consist of a wide range of frequencies. During the wave propagation, the shape of the response might change since the wave velocities depend on the frequency, and some waves travel faster than the others [7]. If the velocities are too close, waves cannot be identified clearly. Therefore, it is important to excite wave modes which have distinct phase and group velocities.

Figure 3.4 shows the dispersion curves for pipes have same wall thickness $t = 1$ mm and different outer radius, which are 13 mm, 25 mm, 50 mm and 136 mm respectively. From Figure 3.4, it is observed that the first longitudinal wave mode L(0,1) has the wave velocity close to the wave speed $\sqrt{E/\rho}$ [26] in a bar, which is 5159 m/s in this case. With the frequency increasing, the wave velocity of L(0,1) decreases, then gradually increase and approach to a certain velocity. With the increasing of the outer radius of the pipe, L(0,1) drops at lower frequency and the dispersion curves for the pipe get closer to that for plates of the same thickness. From Figure 3.4, we can see that the dispersion curves are not sensitive to the change of radius if the outer radius is larger than 50 mm.

3.3 Analytical Solution

By numerical calculation, dispersion curves for a pipe that has the outer radius of 136 mm and the thickness of 1 mm are obtained as shown in Figure 3.5. As mentioned above, for a hollow cylinder, the fundamental longitudinal mode $L(0,1)$ begins at zero frequency, and as the frequency increases, the phase velocity increases and converges to a certain value. The second mode $L(0,2)$ begins at a certain frequency with an infinite phase velocity. For higher frequency, the velocity significantly reduces to Young's velocity $\sqrt{E/(\rho(1-\nu^2))}$ [26]. As shown in Figure 3.5, the $L(0,2)$ mode velocity approaches to Young's velocity in the frequency range from 0 to 1 MHz, while $L(0,1)$ is more dispersive in the same frequency range. In addition, as an axisymmetric mode in pipe-like structures, the $L(0,2)$ mode wave travels through the thickness of the pipe wall, which makes it useful for detecting the circumferential defects [11].

A pipe structure is considered as shown in Figure 1.5(b). Tangential surface traction is applied on the outer surface of the pipe at $z = 0.1$ m and $z = -0.1$ m, respectively, and a Morlet signal is applied as an input as shown in Figure 3.6 (a). The amplitudes of Fourier coefficients of the input are plotted in Figure 3.6 (b). The temporal response is calculated analytically at z= 0.2 m (0.1 m away to the excitation coordinate at $z = 0.1$ m). By substituting the wavenumbers for each excitation frequency to Eq. (3.32), the displacement fields are calculated, and the longitudinal and radial displacements are plotted in Figures 3.7 (a) and 3.7(b), respectively.

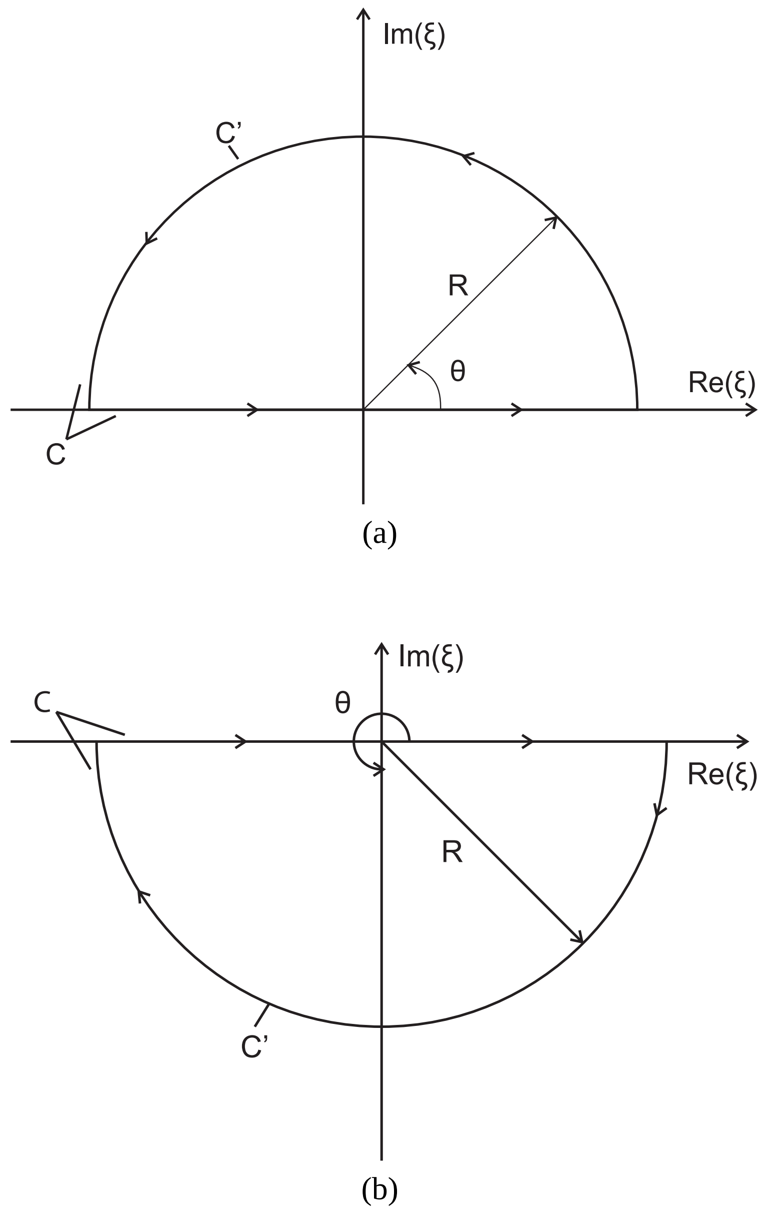

Figure 3.1: Contours for complex domain integration: (a) upper semicircle, and (b) lower semicircle

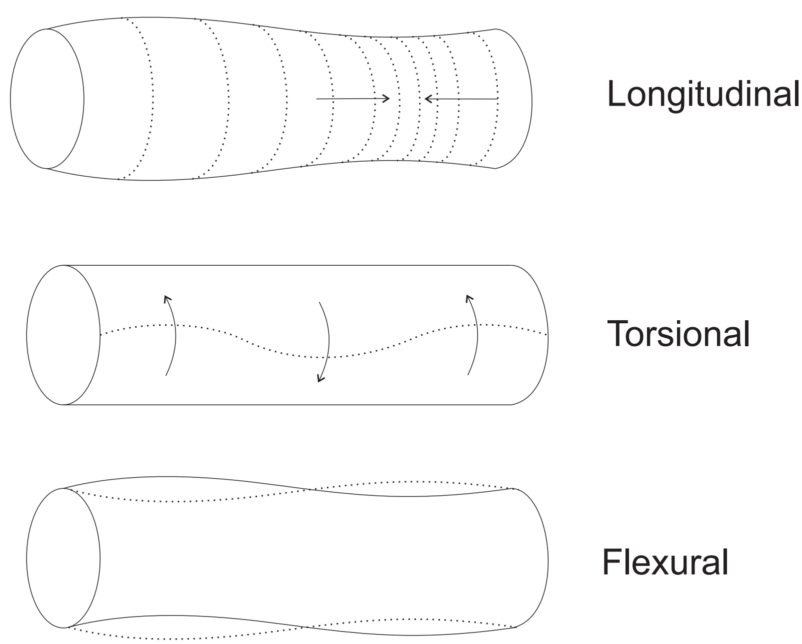

Figure 3.2: Different wave modes in a cylindrical system.

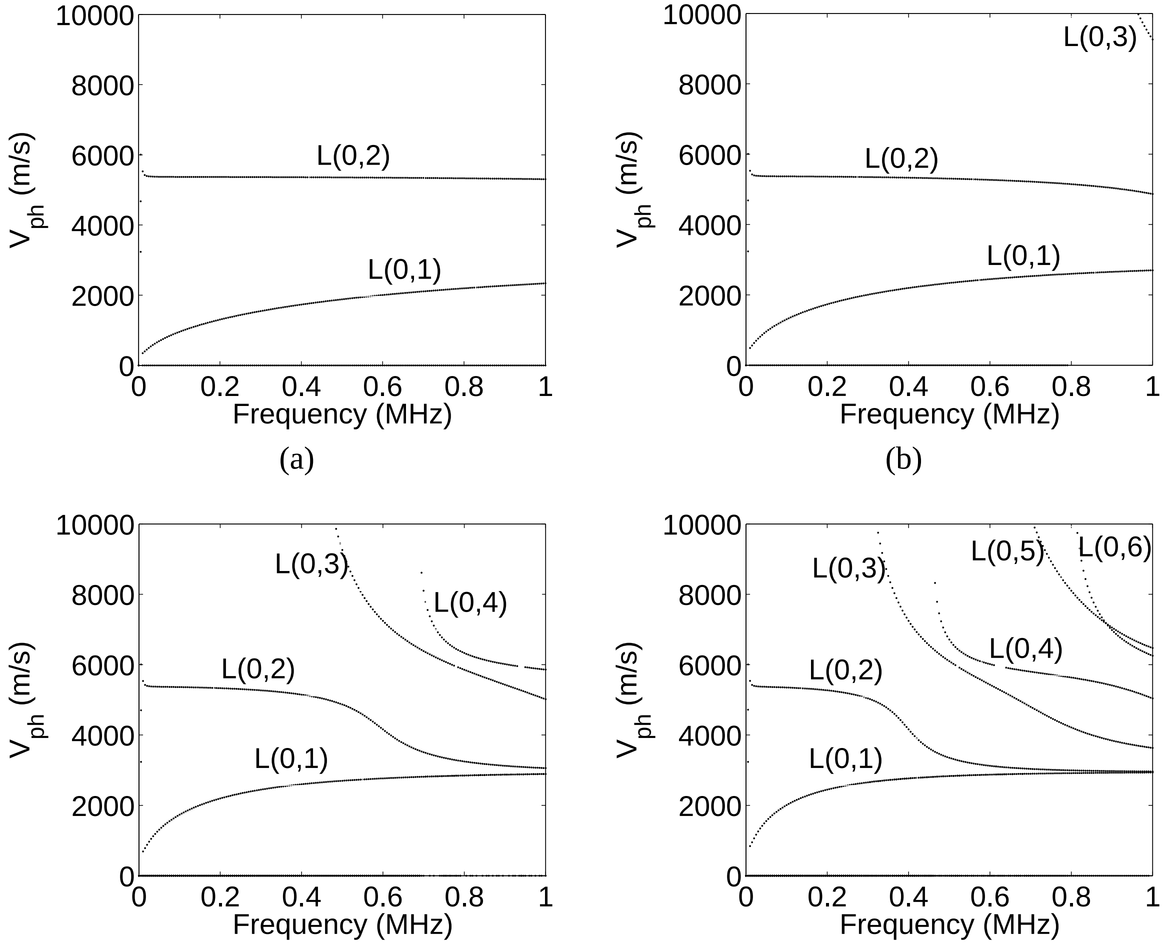

(a) (b)

(c) (d)

Figure 3.3: Dispersion curves for pipes of the outer radius $c_O = 136$ mm with the thicknesses (a) $t = 1$ mm and (b) $t = 2$ mm, (c) $t = 4$ mm and (d) $t = 6$ mm, respectively.

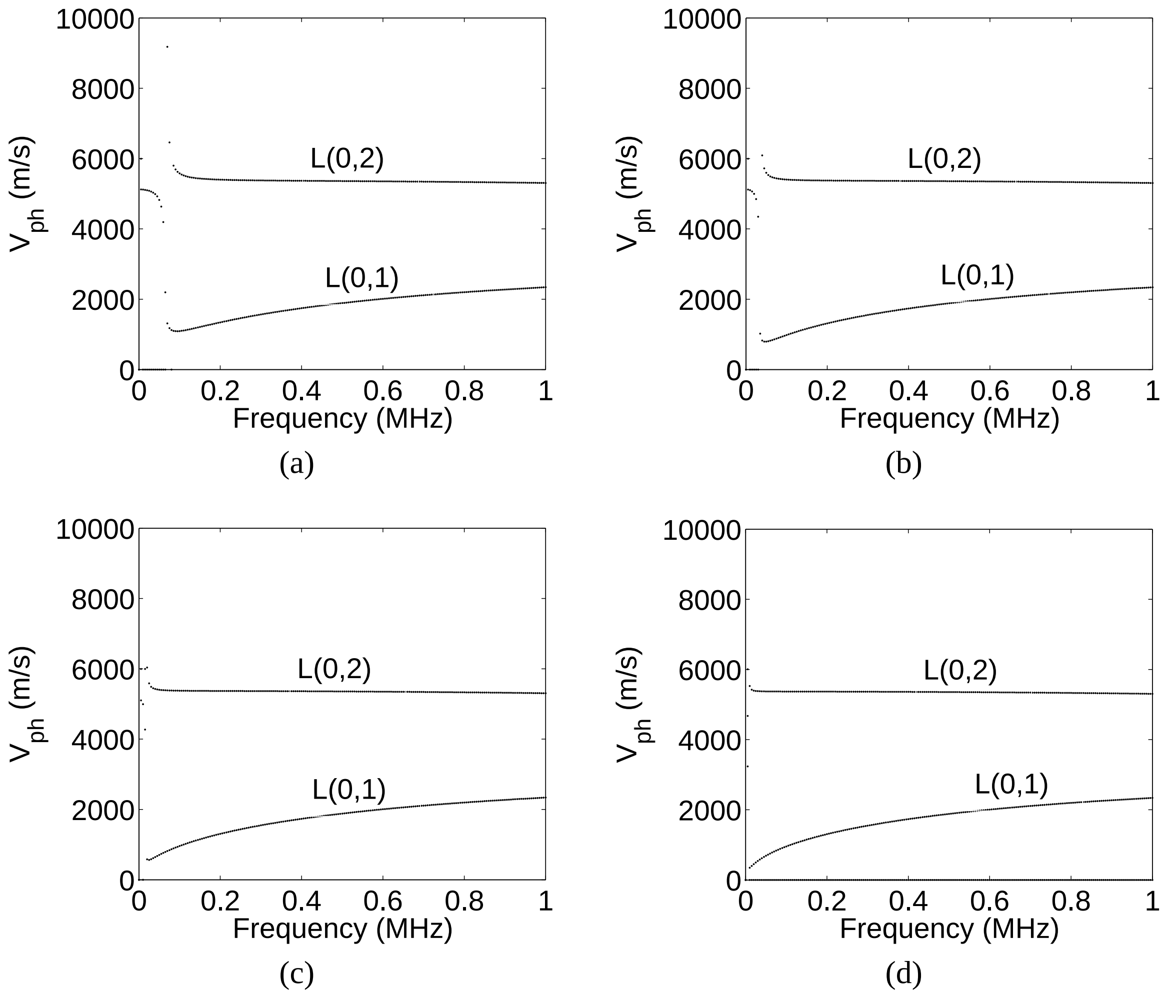

Figure 3.4: Dispersion curves of pipes of the thickness $t = 1$ mm with the outer radii (a) $c_O = 13$ mm and (b) $c_O = 25$ mm, (c) $c_O = 50$ mm and (d) $c_O = 136$ mm, respectively

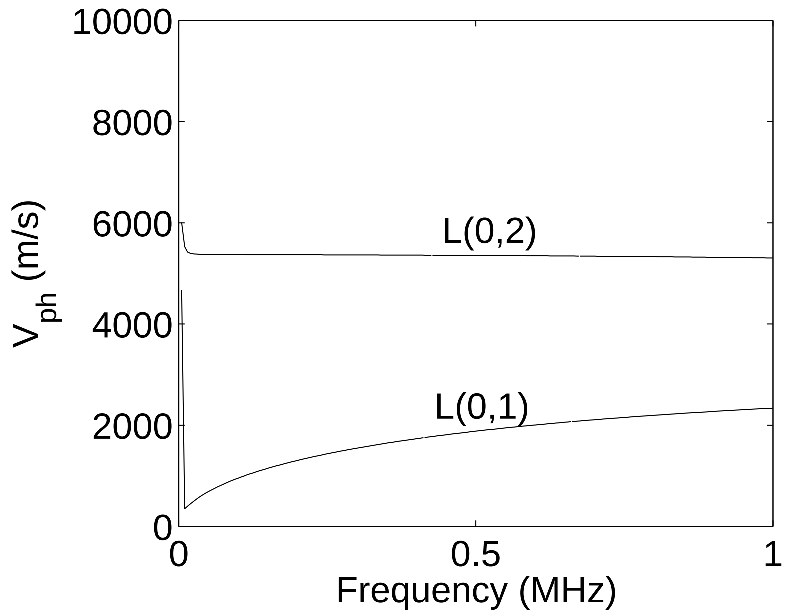

(a)

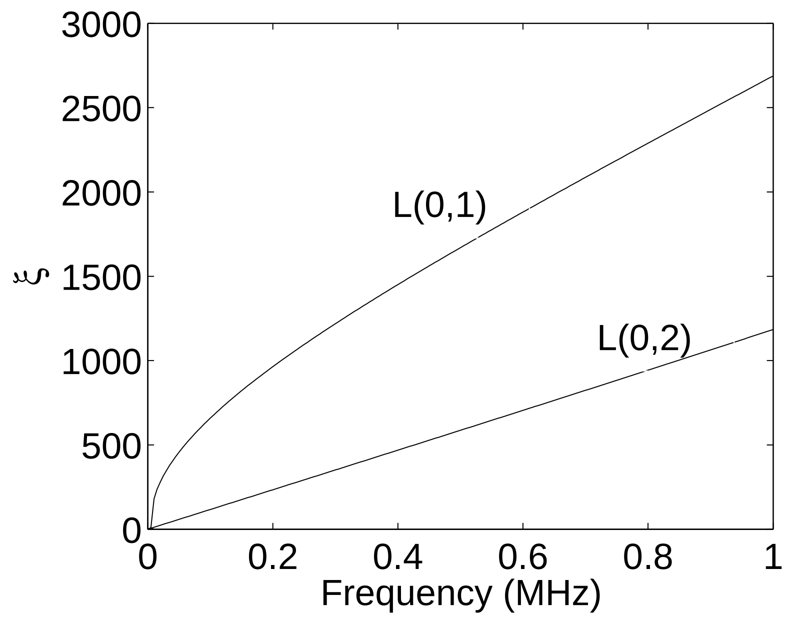

(b)

Figure 3.5: Dispersion Curve of a pipe with $r_O = 136$ mm and $t = 1$ mm: (a) v_{ph} versus f and (b) ξ versus f.

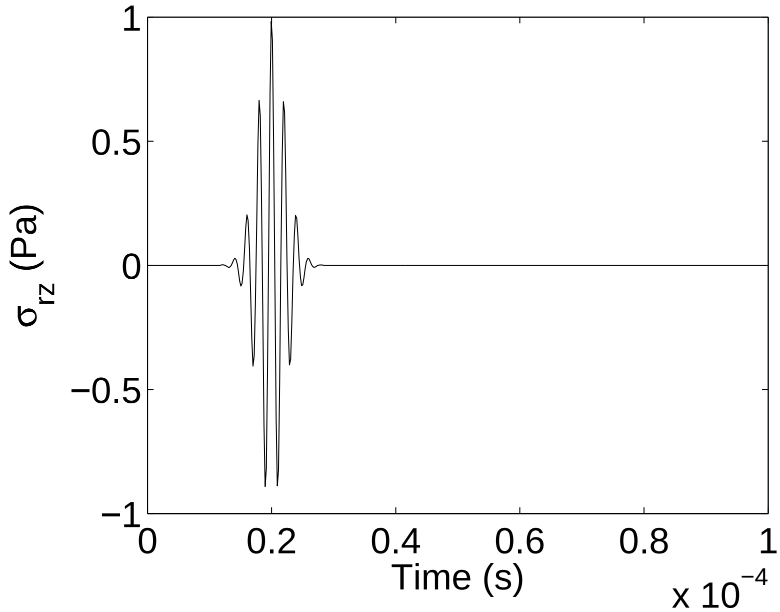

(a)

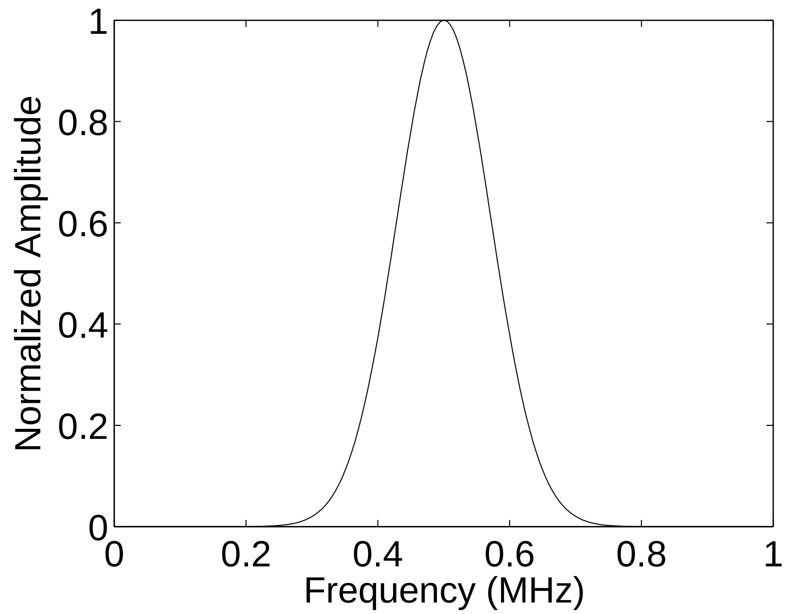

(b)

Figure 3.6: (a) Tangential traction in time domain and (b) magnitudes of Fourier coefficients.

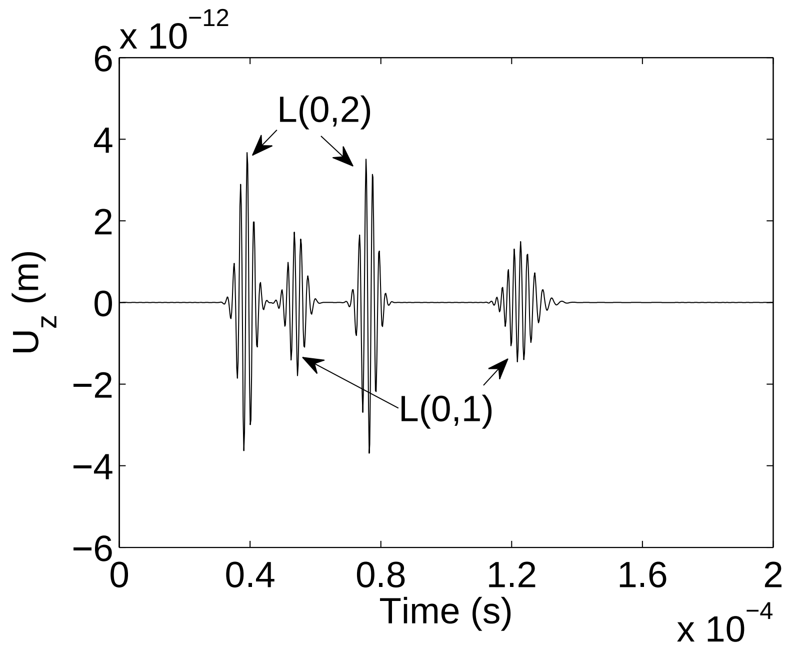

(a)

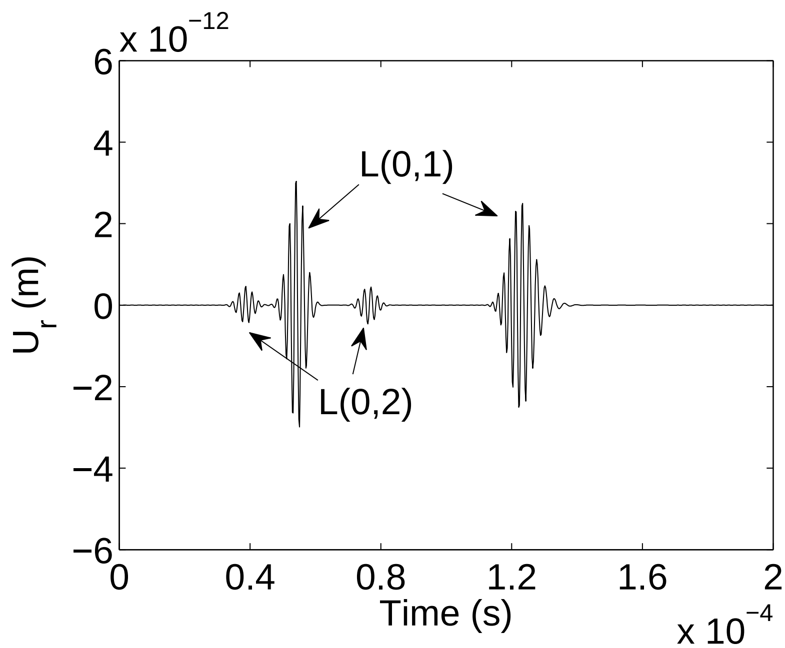

(b)

Figure 3.7: Displacements on the outer surface of a pipe with $c_O = 136$ mm and $t = 1$ mm: (a) u_z and (b) u_r on the outer surface.

Chapter 4

Numerical Simulation

4.1 Finite Element Formulations

The finite element formulation for the wave propagation system is expressed by the equation of motion as [5]:

$$\sigma_{ij,j} + f_i^B = \rho \ddot{u}_i \tag{4.1}$$

where σ_{ij} is the stress component, f_i^B is the body force, ρ is the mass density and u_i is the displacement component.

The stress boundary condition and the displacement boundary condition are expressed respectively as:

$$\begin{aligned} \sigma_{ij} n_j &= F_i^{S_f}, \\ u_i &= u_i^{S_u}. \end{aligned} \tag{4.2}$$

Applying principle of virtual work on Eq. (4.1), we have

$$\int_V (\sigma_{ij,j} + f_i^B - \rho \ddot{u}_i) \bar{u}_i dV = 0. \tag{4.3}$$

By applying divergence theorem, which is expressed as:

$$(\sigma_{ij}\bar{u}_i)_{,j} = \sigma_{ij,j}\bar{u}_i + \sigma_{ij}\bar{u}_{i,j}. \tag{4.4}$$

Eq. (4.3) is rewritten as:

$$\int_S \sigma_{ij}\bar{u}_i n_j dS + \int_V f_i^B \bar{u}_i dV - \int_V \rho\ddot{u}_i\bar{u}_i dV - \int_V \sigma_{ij}\bar{u}_{i,j} dV = 0. \tag{4.5}$$

Substituting Eq. (4.2) to Eq. (4.5), the weak formulation is obtained as:

$$\int_S F_i^{S_f} \bar{u}_i dS + \int_V f_i^B \bar{u}_i dV - \int_V \rho\ddot{u}_i\bar{u}_i dV - \int_V \sigma_{ij}\bar{u}_{i,j} dV = 0. \tag{4.6}$$

By applying Hook's Law,

$$\sigma_{ij} = C_{ijkl}\epsilon_{kl} \tag{4.7}$$

and considering the symmetries of the stress tensor, we have

$$\int_S F_i^{S_f} \bar{u}_i dS + \int_V f_i^B \bar{u}_i dV - \int_V \rho\ddot{u}_i\bar{u}_i dV - \int_V C_{ijkl}\epsilon_{kl}\bar{\epsilon}_{ij} dV = 0. \tag{4.8}$$

The displacement field $\mathbf{u}$ and strain vector $\boldsymbol{\epsilon}$ is expressed by introducing the shape function $\mathbf{H}_u$ and the strain-displacement matrix $\mathbf{B}$ as:

$$\begin{aligned} \mathbf{u} &= \mathbf{H}_u\mathbf{U}, \\ \boldsymbol{\epsilon} &= \mathbf{B}\mathbf{U}. \end{aligned} \tag{4.9}$$

where $\mathbf{U}$ is the nodal displacement matrix. Then, we have Eq. (4.8) in the matrix form as

$$\bar{\mathbf{U}}^T \int_S \mathbf{H}_u^T \mathbf{F}^S dS + \bar{\mathbf{U}}^T \int_V \mathbf{H}_u^T \mathbf{f}^B dV - \bar{\mathbf{U}}^T \int_V \rho \mathbf{H}_u^T \mathbf{H}_u dV \ddot{\mathbf{U}} - \bar{\mathbf{U}}^T \int_V \mathbf{B}^T \mathbf{C} \mathbf{B} dV \mathbf{U} = 0. \tag{4.10}$$

By eliminating $\bar{\mathbf{U}}^T$, we have

$$\int_S \mathbf{H}_u^T \mathbf{F}^S dS + \int_V \mathbf{H}_u^T \mathbf{f}^B dV - \int_V \rho \mathbf{H}_u^T \mathbf{H}_u dV \ddot{\mathbf{U}} - \int_V \mathbf{B}^T \mathbf{C} \mathbf{B} dV \mathbf{U} = 0. \tag{4.11}$$

Rewriting Eq. (4.11) as:

$$\mathbf{M}\ddot{\mathbf{U}} + \mathbf{K}\mathbf{U} = \mathbf{F}, \tag{4.12}$$

where $\mathbf{M}$ is the mass matrix, $\mathbf{K}$ is the stiffness matrix and $\mathbf{F}$ is the force vector. They are expressed respectively as:

$$\begin{aligned} \mathbf{M} &= \int_V \rho \mathbf{H}_u^T \mathbf{H}_u dV, \\ \mathbf{K} &= \int_V \mathbf{B}^T \mathbf{C} \mathbf{B} dV, \\ \mathbf{F} &= \int_S \mathbf{H}_u^T \mathbf{F}^S dS + \int_V \mathbf{H}_u^T \mathbf{f}^B dV. \end{aligned} \tag{4.13}$$

4.2 Comparison of Numerical and Analytical Results

Numerical simulations are carried out using the finite element method. A pipe of the length L = 3 m, the inner radius c_i = 0.135 m, and the thickness t = 1 mm is discretized with eight-node solid elements. The material is linear elastic, Young's Modulus $E = 206 \times 10^9 Pa$, and Poison's Ratio $\nu = 0.3$. The excitations are applied at z = 0.1 m and z = -0.1 m, and the measuring point is located at z = 0.2 m.

Figure 4.1 (a) shows an example of discretized finite element model and Figure 4.1 (b) shows an element of the model. There are two sets of mesh sizes used in this study. Figure 4.1 (b) demonstrated the smaller sizes, which in the longitudinal, circumferential, and radial directions are 0.25 mm, 10.7 mm, and 0.5 mm, respectively. Another set of mesh sizes are 1 mm in axial direction, 10.7 mm in circumferential direction and 0.5 mm in radial direction. The time step is selected to be 3E-8 s to confirm the stability of the solution. Figure 4.2 shows the comparison of the analytical and numerical results using two different mesh sizes. From the figure, we observe that the result from smaller mesh sizes matches better with the analytical solution than that from the larger sizes. In both Figure 4.2 (a) and (b), the first two wave packages of L(0,2) and L(0,1) modes, respectively, are developed by the excitation at $z = 0.1$ m, while the following two waves are from excitation at $z = -0.1$ m. It is observed that L(0,1) mode waves are more dispersive and the magnitudes are smaller than those of L(0,2) mode waves.

Note that the mesh size in the circumferential direction dose not influence the magnitude and the arrival time of the signal significantly. It is because that the excitations are applied symmetrically in circumference, which makes the excited waves do not propagate in that direction. However, the arrive times of waves are quite sensitive to the mesh size in axial direction. Different mesh sizes, 1 mm and 0.25 mm, were used to enhance the accuracy of arrival time. For 1 mm mesh size, the arrival times of L(0,2) from the numerical simulation are close to those from the analytical solution, while the arrival times of L(0,1) from the two methods vary by about 5% for the signal excited at $z = -0.1$ m. For 0.25 mm mesh size, the wave packages of L(0,2) from analytical and numerical methods are well matched for both signals came from near and far excitations. In Figure 4.2 (b), the calculated arrival times of $L(0,1)$ mode waves by the excitation at $z = -0.1$ m

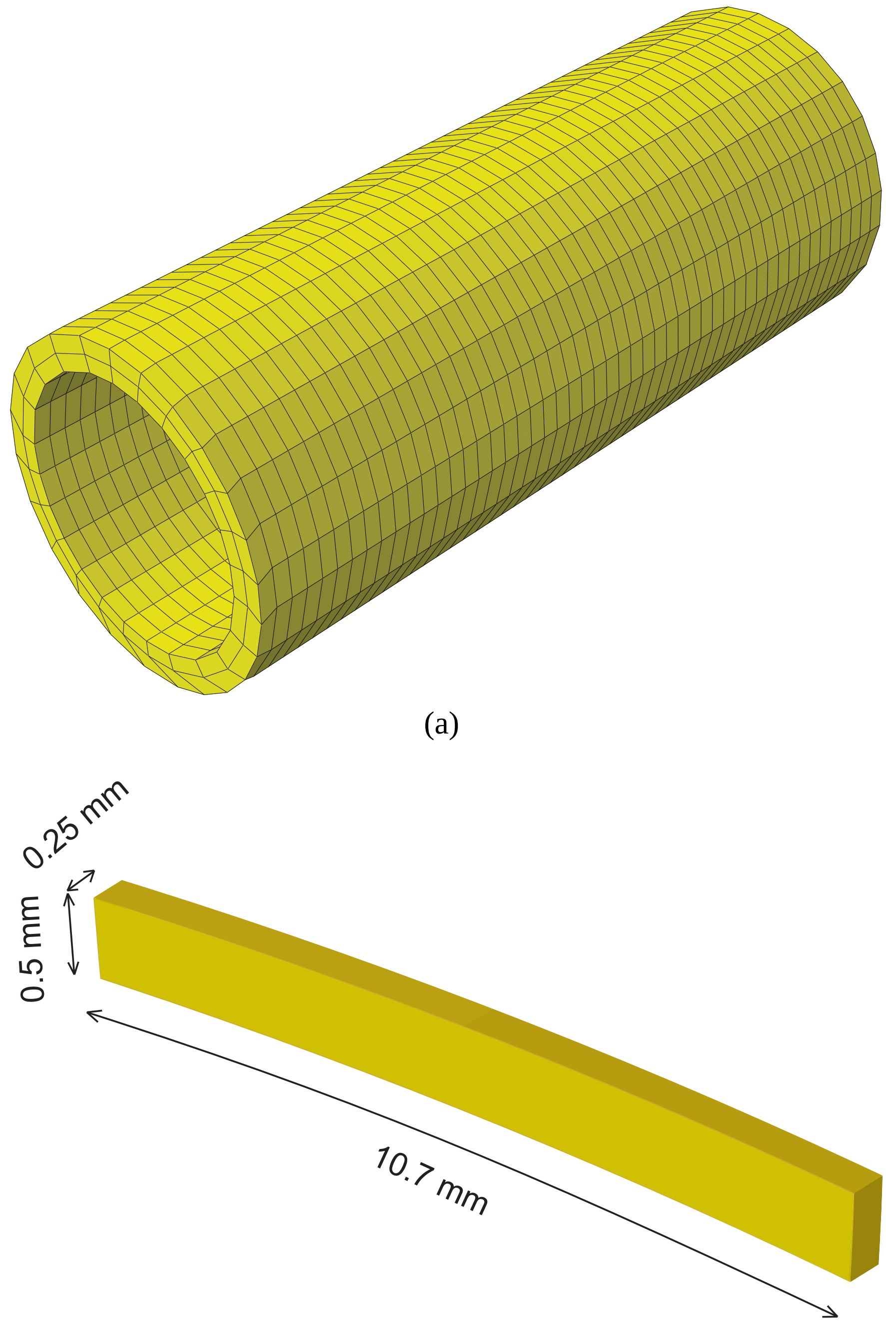

Figure 4.1: (a) An example of discretized FE model, and (b) an element of the model.

are about $122.8\ \mu s$ and $122\ \mu s$, respectively by the analytical and numerical calculations, and the variation in group velocity of L(0,1) mode is less than 1%.

4.3 Lamb Waves in Pipes with Defects

Due to the higher accuracy of the smaller mesh sizes, it is used for the simulations in this section. For the investigation of the defects in pipe-like structures, the comparison of the signals from an intact structure and a damaged structure might enable the quantitative estimation of the damage. As shown in Figure 4.3, a defect is modeled by deleting ten elements along the circumferential direction at $z = 0.4$ m. The defect is through the thickness of the pipe, and the defect width is 1 mm in the axial direction of the pipe. Excitations are applied at $z = 0.1$ m and $z = -0.1$ m, and the signals are measured at 3 different locations, which are $z = 0.25$ m, $z = 0.45$ m and $z = 0.6$ m.

Figure 4.4 shows the received signals from the intact pipe and the damaged pipe. The waves measured at a point ($z = 0.25$ m) between the excitation location ($z = 0.1$ m) and the defect ($z = 0.4$ m) are plotted in Figure 4.4 (a). It is observed that the waves are reflected from the defect, and the magnitudes of the reflected waves are similar to the magnitudes of the incident waves in the intact pipe. The waves shown in Figure 4.4(b) are measured at $z = 0.45$ m (0.05 m away from the defect). Compared with the waves measured in the intact pipe, the magnitudes are reduced significantly although the times-of-flight are of slight difference. The waves still can reach to the measuring point, but the reflection and diffraction around the defect reduce the wave energy significantly. Figure 4.4 (c) shows the displacements measured at $z = 0.6$ m (0.2 m away from the defect). The influence of the defect is reduced, compared to the result shown in Figure 4.4 (b). The magnitudes of the displacements still decrease, but the ratio of the signal from the damaged pipe to the signal from the intact pipe is larger than the ratio observed at $z = 0.45$ m.

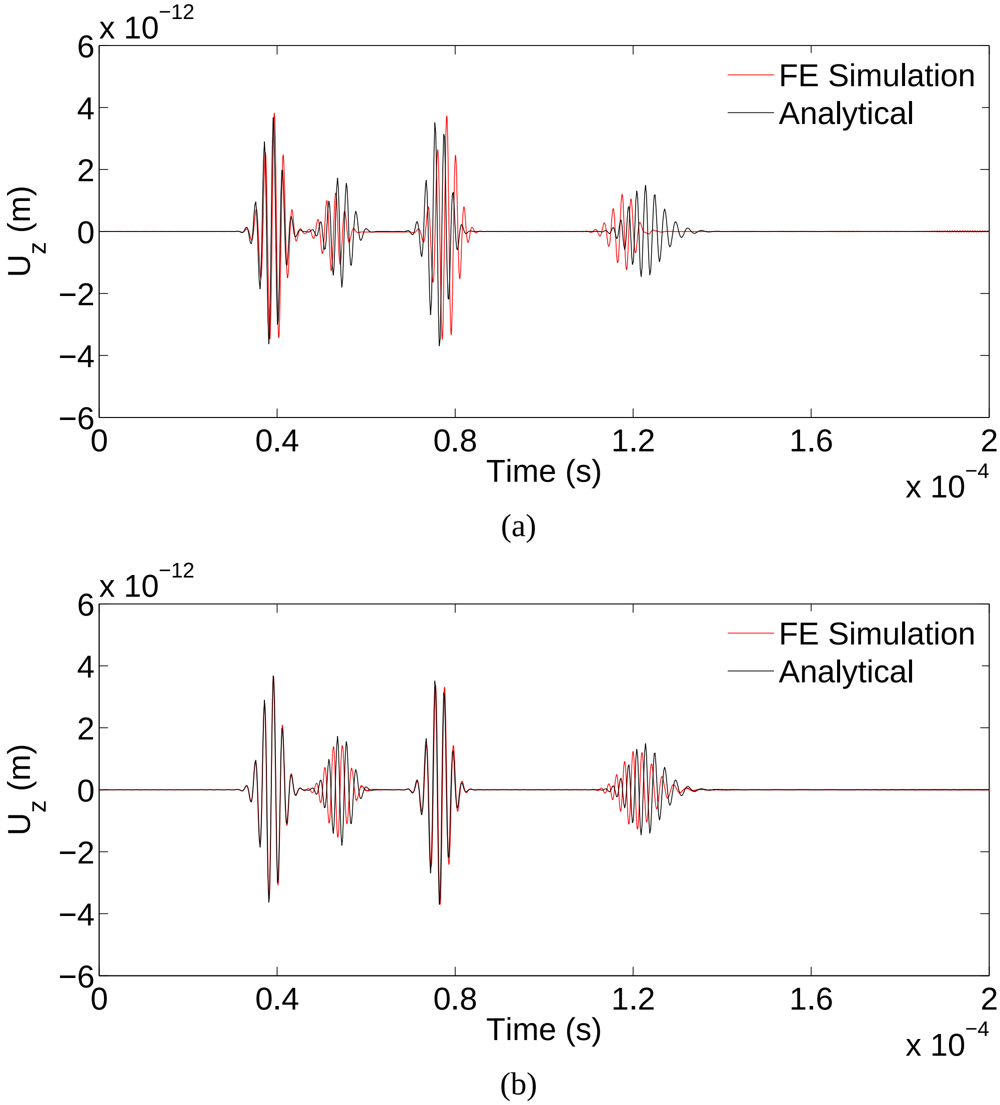

Figure 4.2: Comparison of displacement field u_z on the outside surface of a pipe with c_O= 136 mm and t= 1 mm using mesh size in z direction of: (a) 1 mm, and (b) 0.25 mm.

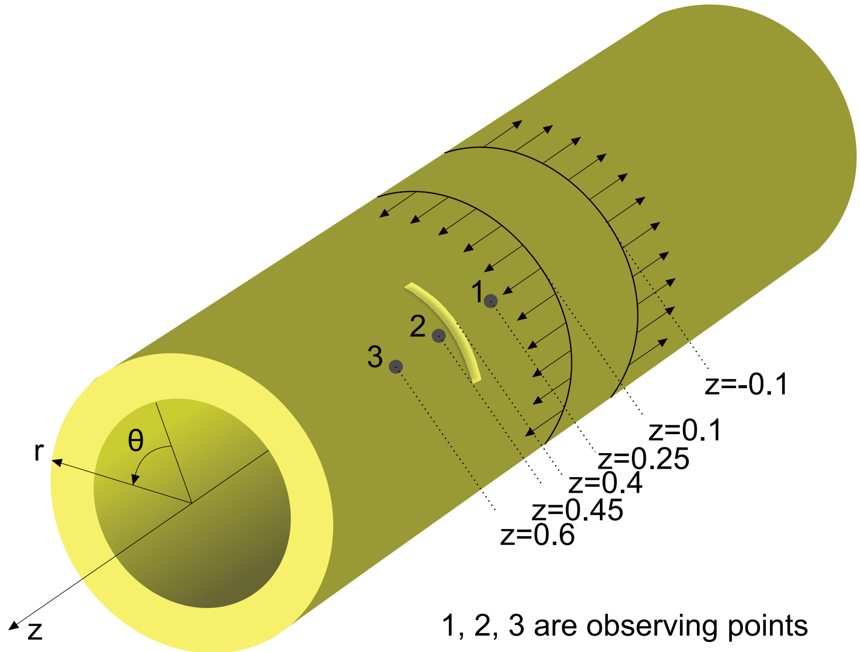

Figure 4.3: Schematic of a pipe with a defect at z= 0.4 m.

4.4 Parametric Study of Responses for Different Defect Sizes

In this section, we use the finite element method to simulate Lamb wave propagation in damaged pipes with different sizes of defects, including the differences in defect width and depth. Our goal is to investigate how the defect size influences the response signals. Figure 4.5 shows the comparison of the signals resulting from pipes with defect widths of 2 mm and 1 mm, respectively. Both defects span through the wall thickness of the pipes, and their sizes in circumferential direction are 107 mm. The FE model used in this comparison is the same as the model used in the previous section. The signal is recorded at the location $z = 0.6$ m. It is observed that the width of the defect has negligible influences on the arrival times as well as on the magnitudes of the waves. Although the width of the defect increases, the dimension is still very small compared with the distance between the measuring point and the defects, thus the change is not large enough to induce any changes into the received signals.

Figure 4.6 shows the comparison of the signals obtained from intact pipes, and the pipes with different defect depth of 0.25 mm, 0.5 mm, 0.75 mm and 1 mm respectively. In order to investigate the waves from defects of different depths, the thickness of the pipe is needed to be divided into 4 layers. Smaller mesh sizes require more time and computer memory to conduct the simulations. Therefore, a pipe of smaller size in the longitudinal direction is used in this section: the thickness of the pipe is 1 mm, while the length of the pipe is modified to 1.4 m. The mesh sizes of the model are 0.25 mm in radial direction, 0.25 mm in axial direction and 10.7 mm in circumferential direction. The defect is located at $z = 0.2$ m, and the measuring point is at $z = 0.35$ m.

From Figure 4.6, we observe that the depth of the defect is inversely proportional to the magnitude of the received incident signals. It is easy to understand that the deeper the defect, more waves are interfered and the magnitudes of the signals are decreased. Meanwhile, we observe that the depth of the defect does not have much influence on the arrival times of the signals. Another interesting thing is that when the depth of the defect is smaller than the thickness of the pipe, additional wave modes are generated in the pipe walls. Those wave modes might be generated by the diffractions of the incident wave modes on the defects. Figure 4.6 (d) shows the comparisons between the 4 signals from pipes with defects of different depths on them. It is observed that the magnitudes of refracted signals increase a lot when the defect depth gets deeper from 0.25 mm to 0.5 mm, while they remain almost the same when the defect depth goes from 0.5 mm to 0.75 mm. The possible reason is that the particle vibration on the surface of the pipe is much smaller than the vibration inside the pipe wall, which makes the signals larger when they are refracted in the middle of the pipe wall.

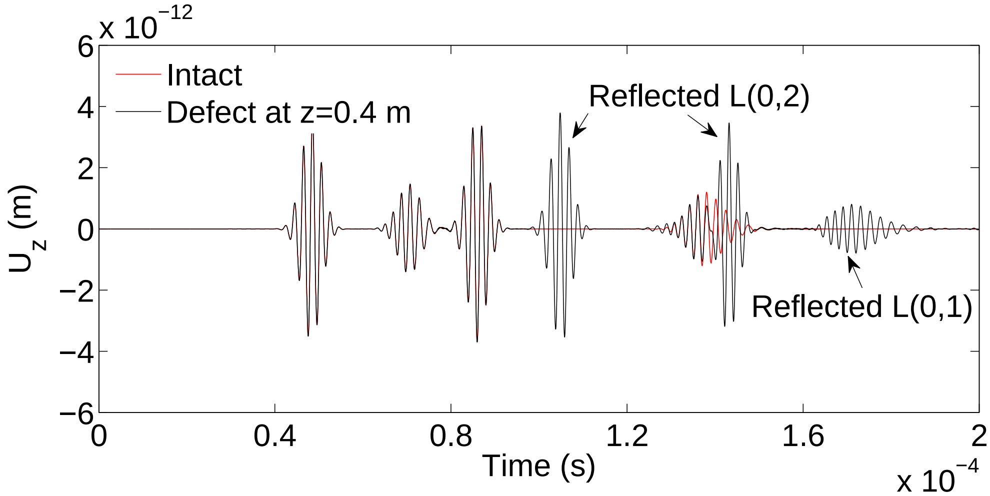

(a)

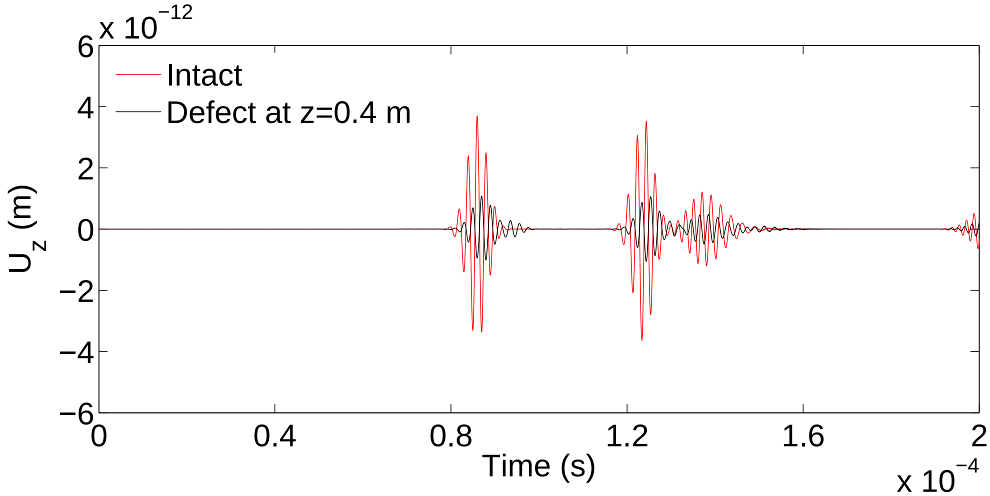

(b)

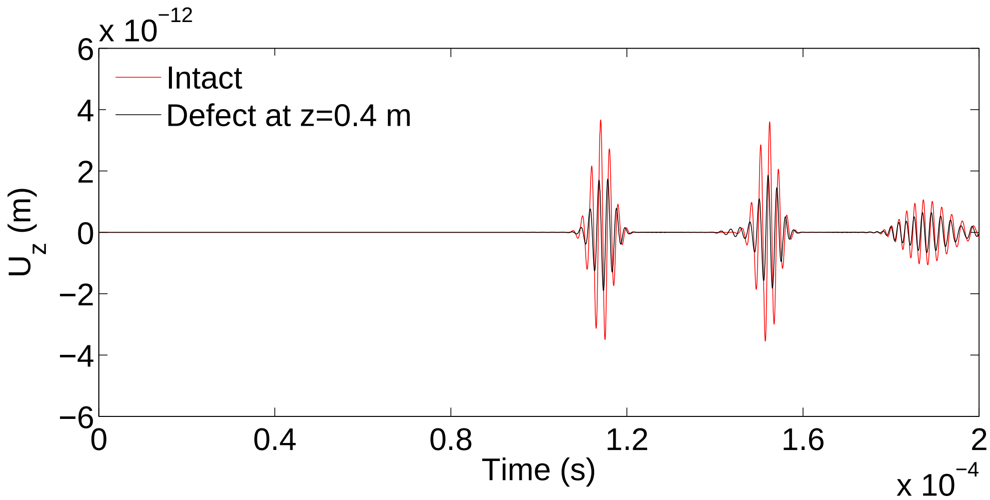

(c)

Figure 4.4: Comparison of displacements measured in pipes (one is intact, and the other is damaged): Displacements u_z are measured (a) at z= 0.25 m, (b) at z= 0.45 m, and (c) at z= 0.6 m.

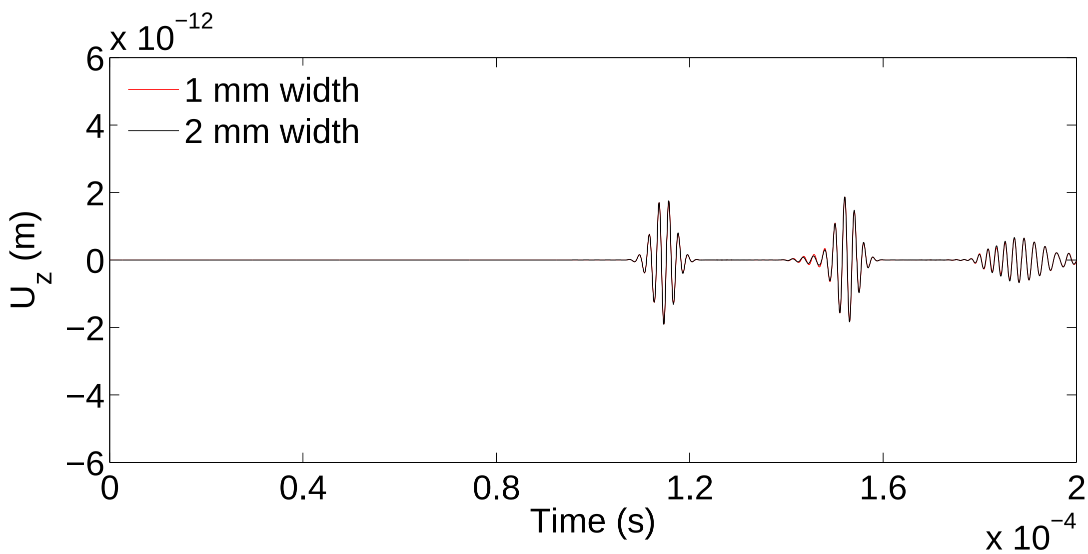

Figure 4.5: Comparison of displacements measured at $z = 0.6$ m on the outer surface of pipes with defect width of 1 mm vs 2 mm.

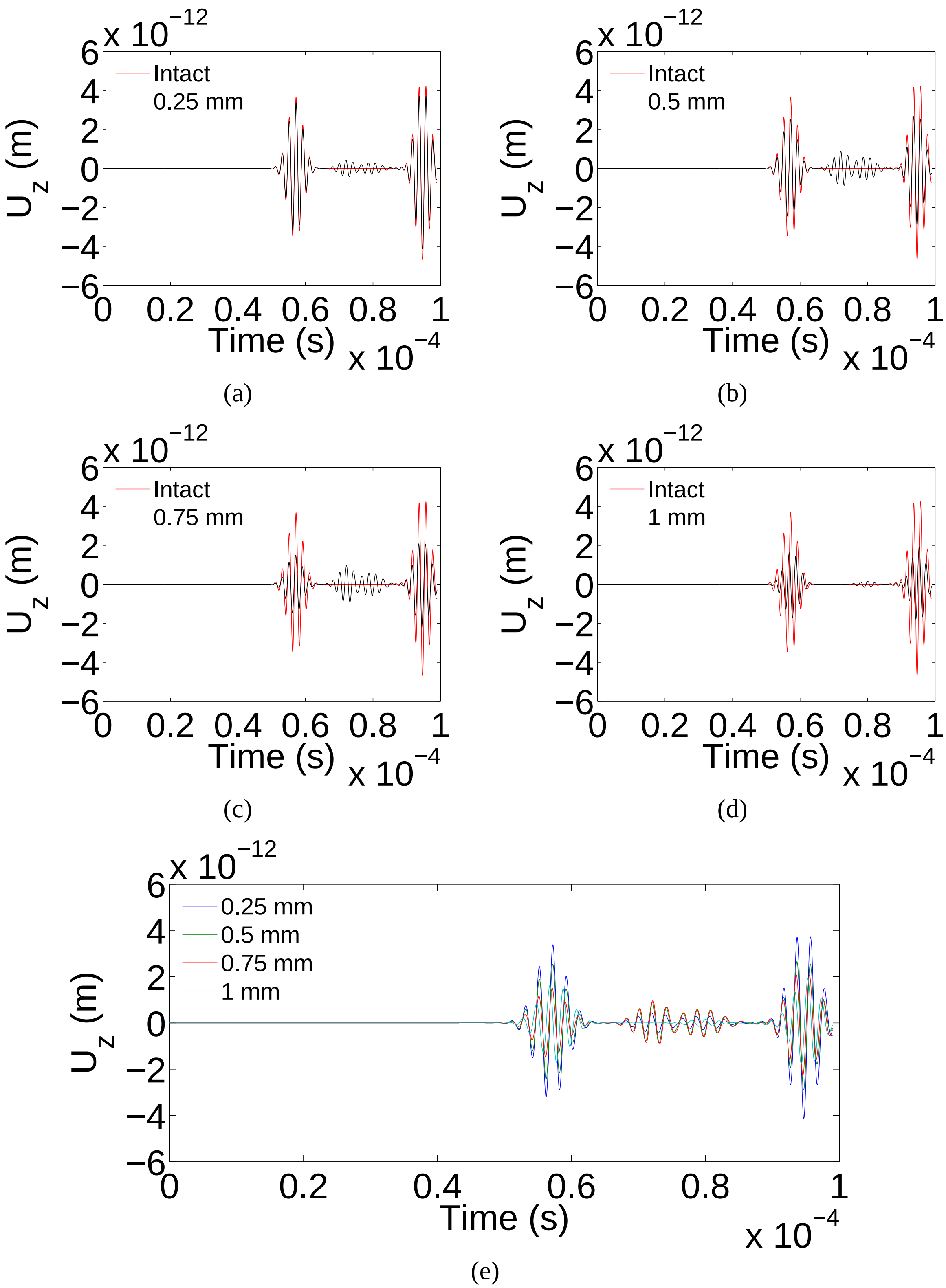

Figure 4.6: Comparison of displacements measured at $z = 0.35$ m on the outer surface of pipes with: (a) non-defect vs defect depth of 0.25 mm; (b) non-defect vs defect depth of 0.5 mm; (c) non-defect vs defect depth of 0.75 mm; (c) non-defect vs defect depth of 1 mm; (e) defect depth of 0.25 mm, 0.5 mm, 0.75 mm and 1 mm.

Chapter 5

Summary and Conclusions

This thesis focuses on investigating the characteristics of Lamb wave propagation in pipe-like structures. Both theoretical analysis and numerical simulation are conducted to study the Lamb wave behavior under wide-band excitations which are symmetrically applied on the outer surface of a pipe in circumferential direction. The analytical and numerical results are compared, and the accuracy of the finite element model is verified for further investigation of Lamb waves in damaged pipelines.

In Chapter 1, a brief introduction of Structural Health Monitoring and Non-Destructive Evaluation is conducted, and the motivation and objectives of this thesis are elaborated as well. The detailed contents of Chapter 1 include:

- Define the concept of damage in structures;
- Explain the necessities of SHM and DNE methodologies;
- Introduce three commonly used NDE methods;
- Present the advantages of Lamb wave as a relatively ideal tool for ultrasonic testing;
- Introduce the developments of the theories and the applications of Lamb waves in NDE area;
- Explain the motivation and objectives of this research.

Lamb wave propagation in plates is studied in Chapter 2. The main work conducted in Chapter 2 includes:

- Introduce two types of Lamb wave modes in plates;
- Explain two criteria of choosing proper wave modes for structural integrity inspection;
- Outline the derivation of characteristic equations of Lamb waves in plates;
- Plot the dispersion curves of a steel plate of 1 mm thick using PACshare DispersionPlus Curves;
- Verify the accuracy of the numerical simulation of wave propagation in an aluminum plate by comparing with published experimental data.

Chapter 3 and Chapter 4 investigated wave propagation in pipe-like structures both analytically and numerically. Main contents in these two chapters are shown as following:

- Show the detailed derivation of dispersion equation of Lamb waves in pipe-like structures;
- Plot the dispersion curves of Lamb waves in pipelines, and compared them between pipes with different wall thicknesses and outer radii;
- Calculate the displacement fields on the outer surface of an intact pipeline;
- Simulate Lamb wave propagation in an intact pipeline and compared the numerical results with the analytical results;
- Conduct parametric study to investigate the influences of defect sizes on Lamb wave behaviors in pipe-like structures.

The derivation of dispersion equation of Lamb waves in pipe-like structures is followed the initial work conducted by Gazis in 1959. After the dispersion equation is derived, the dispersion curves are plotted for pipes with different geometries by solving the dispersion equations. The comparisons show the sensitivity of the dispersion curves to the geometry of the pipelines. It is observed that, as the outer radius of a pipe increases, the wave velocity of L(0,1) mode decreases at lower frequency and the dispersion curves of a pipe get closer to those of a plate with the same thickness and material properties. On the other hand, as the wall thickness of a pipe increases, more wave modes exist in the pipe. To obtain the displacement fields generated by Lamb waves in an intact pipe, a steel pipe with 1 mm wall thickness is selected for analytical calculation and numerical simulation. Excitations are applied as shear tractions at z = -0.1 m and z = 0.1 m on the outer surface of the pipeline and the received signals, which are the displacement fields, are measured at location $z = 0.2$ m, where z denotes the coordinate in axial direction of the pipe. The excitation is a wide-band shear traction with center frequency f_C= 500 kHz. The comparison between the results from the two methods shows good agreement, especially for the wave mode L(0,2), and the accuracy of the numerical model is verified.

After the accuracy is confirmed, finite element simulations are carried out to study Lamb waves in damaged pipelines, and the results are compared with the waves calculated in the intact pipe. From the comparison, it is observed that waves are reflected from the edges of the defects. The magnitudes of the waves are more sensitive to the defect than the time delays, and the effect is less eminent when the distance from the defect to the measuring point increases. A parametric study is conducted to compare the signals from damaged pipes with different defect widths and depths. The signals obtained from the damaged pipes with defect widths of 1 mm and 2 mm are studied in this thesis. From the signals, it is observed that the longitudinal modes in the pipeline are not sensitive to the widths of the defects, and the signals resulting from the two defects have trivial difference both in magnitude and arrival time. On the other hand, signals from pipes with different defect depths show significant differences. The magnitudes of the incident waves are inversely proportional to the depths of defects. In addition, from the comparisons one can observe that more wave modes are introduced to the damaged pipelines due to the diffractions by the defects. The magnitudes of the waves generated inside the pipe walls are larger than those generated near the surface of the pipes.

BIBLIOGRAPHY

BIBLIOGRAPHY

[1] http://tophealthmonitors.info/2012/02/structural-health-monitoring/.

[2] D.N. Alleyne. The nondestructive testing of plates using ultrasonic lamb waves. *Phd, Imperial College of Science Technology and Medicine, London*, 1991.

[3] C. Aristegui, MJS Lowe, and P. Cawley. Guided waves in fluid-filled pipes surrounded by different fluids. *Ultrasonics*, 39(5):367–375, 2001.

[4] B.A. Auld. *Acoustic fields and waves in solids*. RE Krieger, 1990.

[5] K.J. Bathe. *Finite element procedures*. Prentice Hall Englewood Cliffs, NJ, 1996.

[6] E.O. Brigham and R.E. Morrow. The fast Fourier transform. *Spectrum, IEEE*, 4(12):63–70, 1967.

[7] P. Cawley and D. Alleyne. The use of Lamb waves for the long range inspection of large structures. *Ultrasonics*, 34(2):287–290, 1996.

[8] C. Chree. The equations of an isotropic elastic solid in polar and cylindrical coordinates their solution and application. *Transactions of the Cambridge Philosophical Society*, 14:250, 1889.

[9] A.C. Cobb, J.E. Michaels, and T.E. Michaels. Ultrasonic structural health monitoring: a probability of detection case study. In *Review of Progress in QNDE, 28A, edited by DO Thompson and DE Chimenti, AIP Conference Proceedings*, volume 1096, pages 1800–1807, 2009.

[10] Physical Acoustics Corporation. PACshare DispersionPlus Curves, 2011.

[11] J.O. Davies. *Inspection of pipes using low frequency focused guided waves*. PhD thesis, Imperial College London, 2008.

[12] O. Diligent. Interaction between fundamental lamb modes and defects in plates. *Mechanical Engineering*, 2003.

[13] B.W. Drinkwater and P.D. Wilcox. Ultrasonic arrays for non-destructive evaluation: A review. *NDT & E International*, 39(7):525–541, 2006.

[14] C.R. Farrar and K. Worden. An introduction to structural health monitoring. *Philosophical Transactions of the Royal Society A: Mathematical, Physical and Engineering Sciences*, 365(1851):303–315, 2007.

[15] D.C. Gazis. Three-dimensional investigation of the propagation of waves in hollow circular cylinders. I. analytical foundation. *The Journal of the Acoustical Society of America*, 31:568, 1959.

[16] D.C. Gazis. Three-dimensional investigation of the propagation of waves in hollow circular cylinders. II. numerical results. *The Journal of the Acoustical Society of America*, 31:573, 1959.

[17] V. Giurgiutiu and A. Cuc. Embedded non-destructive evaluation for structural health monitoring, damage detection, and failure prevention. *Shock and Vibration Digest*, 37(2):83, 2005.

[18] K.F. Graff. *Wave motion in elastic solids*. Dover Publications, 1975.

[19] D.W. Greve, J.J. Neumann, J.H. Nieuwenhuis, I.J. Oppenheim, and N.L. Tyson. Use of lamb waves to monitor plates: experiments and simulations. In *Proc. SPIE*, volume 5765, pages 281–292, 2005.

[20] R. Holt and J.L. Hartmann. *Adequacy of the U10 & L11 Gusset Plate Designs for the Minnesota Bridge No. 9340 (I-35W over the Mississippi River)*. Federal Highway Administration, Turner-Fairbank Highway Research Center, 2008.

[21] S. Kim, D. Culler, J. Demmel, G. Fenves, S. Glaser, T. Oberhein, and S. Pakzad. Structural health monitoring of the golden gate bridge. *Disponível: http://www. cs. berkeley. edu/˜ binetude/[consulta: Janeiro de 2006]*, 2003.

[22] H. Lamb. On waves in an elastic plate. *Proceedings of the Royal Society of London. Series A*, 93(648):114–128, 1917.

[23] A.I. Markushevich and R.A. Silverman. *Theory of functions of a complex variable*, volume 1. American Mathematical Society, 2005.

[24] J. Miklowitz. The theory of elastic waves and waveguides. *Applied Mathematics and Mechanics*, 22, 1984.

[25] B. Muravin, G. Muravin, and L. Lezvinsky. The fundamentals of structural health monitoring by the acoustic emission method. *Proceedings of the 20th International Acoustic Emission Symposium*, pages 253–258, 2010.

[26] B.N. Pavlakovic. *Leaky guided ultrasonic waves in NDT*. PhD thesis, University of London, 1998.

[27] A. Raghavan and C.E.S. Cesnik. 3-D elasticity-based modeling of anisotropic piezocomposite transducers for guided wave structural health monitoring. *Journal of Vibration and Acoustics*, 129:739, 2007.

[28] L. Rayleigh. On the free vibrations of an infinite plate of homogeneous isotropic elastic matter. *Proceedings of the London Mathematical Society*, 1(1):225–237, 1889.

[29] J.L. Rose. A baseline and vision of ultrasonic guided wave inspection potential. *Transactions-American Society of Mechanical Engineers Journal of Pressure Vessel Technology*, 124(3):273–282, 2002.

[30] J.L. Rose, Y. Cho, and M.J. Avioli. Next generation guided wave health monitoring for long range inspection of pipes. *Journal of Loss Prevention in the Process Industries*, 22(6):1010–1015, 2009.

[31] J.L. Rose, Y. Cho, and J.J. Ditri. Cylindrical guided wave leakage due to liquid loading. *Review of Progress in Quantitative Nondestructive Evaluation*, 13:259–259, 1994.

[32] J.L. Rose and P.B. Nagy. Ultrasonic waves in solid media. *The Journal of the Acoustical Society of America*, 107:1807, 2000.

[33] H.A. Sodano, G. Park, and D.J. Inman. An investigation into the performance of macro-fiber composites for sensing and structural vibration applications. *Mechanical Systems and Signal Processing*, 18(3):683–697, 2004.

[34] H. Sohn, C.R. Farrar, F. Hemez, and J. Czarnecki. *A review of structural health monitoring literature: 1996-2001*. Los Alamos National Laboratory Los Alamos, New Mexico, 2004.

[35] Z. Sun, L. Zhang, and J.L. Rose. Flexural torsional guided wave mechanics and focusing in pipe. *Journal of Pressure Vessel Technology*, 127:471, 2005.

[36] R.L. Taylor. *FEAP–A Finite Element Analysis Program, Version 8.2 User Manual*. University of California at Berkeley, Berkeley, CA, 2008.

[37] I.A. Viktorov. *Rayleigh and Lamb waves: physical theory and applications*. Plenum press New York, 1967.